JOURNAL OF PETROLOGY

Journal of Petrology, 2021, Vol. 62, No. 12, 1–23
https://doi.org/10.1093/petrology/egab088
Advance Access Publication Date: 25 October 2021
Original Manuscript

OXFORD

Ancient Melt-Depletion in Fresh to Strongly Serpentinized Tonga Trench Peridotites

James M.D. Day* and Diana B. Brown

Scripps Institution of Oceanography, University of California San Diego, La Jolla, CA 92093, USA

*Corresponding author. E-mail: jmdday@ucsd.edu

Received 28 April 2021; Revised 18 October 2021; Accepted 19 October 2021

Abstract

Peridotites from the Tonga Trench are some of the deepest-derived and freshest ever obtained from the seafloor. This study reports new bulk-rock major-, trace-, highly siderophile-element (HSE) abundance and $^{187}Os/^{188}Os$ data, as well as major- and trace-element abundances of mineral phases for NOVA88D dredge peridotites. The samples are harzburgites that experienced varying degrees of serpentinization, recorded in their loss on ignition (LOI) values, from zero to 16.7%. Degree of serpentinization in samples is correlated with Na, B, K, Sr, Ca, Rb and U, and weakly correlated with W, Fe, Pb, Cs and Li abundances, but is uncorrelated with other lithophile elements, most especially the rare earth elements (REE). Serpentinization had no systematic effect on the HSE abundances or $^{187}Os/^{188}Os$ compositions in the harzburgites. NOVA88D harzburgites record >18% melt depletion which has resulted in heterogenous distribution of the HSE within the rocks, likely due to retention of these elements within sub-micron sized alloy or sulphide phases. Time of rhenium depletion (T_{RD}) ages, recorded by Os isotopes, average $\sim 0.7 \pm 0.4$ Ga and can be as ancient as 1.5 Ga. Some harzburgite compositions are consistent with minor melt infiltration processes modifying incompatible trace element compositions and Re abundances, with a possible melt infiltration event at ~120 Ma based on ^{187}Re-^{188}Os, prior to the inception of subduction at the Tonga Trench at ~52 Ma. Evidence for ancient melt depletion, combined with limited melt processing since inception of subduction suggests that NOVA88D harzburgites represent melt residues incorporated into the Tonga arc, rather than their geochemical signatures being produced beneath the recent arc. Estimates of fO_2 ($\sim -0.4 \pm 0.4$ ΔFMQ) and olivine-spinel equilibration temperatures for the Tonga Trench samples (830 ± 120 °C) are similar to abyssal peridotites and some Izu-Mariana-Bonin peridotites. These values are unlikely to relate directly to recorded degrees of melt depletion and melt depletion ages in the rocks. Refractory residues from prior melt depletion events are probably common in the convecting mantle, and those with high degrees of melt depletion (>18%) and relatively ancient melt depletion ages (<2 Ga) are likely to have been formed during prior melting processes rather than melting processes within their current tectonic setting. These refractory peridotites can be incorporated into a range of tectonic settings, including into mid-ocean ridges, succeeding arcs, or within the continental lithospheric mantle, where they may play a limited role in melt generation processes.

Key words: Tonga Trench; melt-depletion; Os isotopes; highly siderophile elements (HSE); peridotites; serpentinization; seafloor alteration

INTRODUCTION

Mantle peridotites that have been dredged and drilled or collected as xenoliths from within the ocean basins provide insights into a range of Earth processes and the nature of the convecting mantle. These insights range from understanding melting processes beneath ridges and within subduction zones (e.g. Parkinson *et al.*, 1998; Rampone *et al.*, 1998; Harvey *et al.*, 2006), the importance of oceanic lithosphere in the assembly of continental margins (e.g. Liu *et al.*, 2018; Snortum & Day, 2020), to the definition of the convecting mantle composition (e.g. Snow & Reisberg, 1995; Brandon *et al.*, 2000; Meisel *et al.*, 2001; Müntener & Manatchal, 2006; Becker *et al.*, 2006; Warren, 2016; Day *et al.*, 2017a).

An impediment to progress in these scientific arenas has been serpentinization within oceanic peridotites. Serpentinization results from the hydrothermal alteration of silica-poor, olivine-rich rock in heavily fractured and faulted areas, and commonly occurs beneath mid-ocean ridges, and at plate margins where it is estimated between 10% and 20% of the upper mantle (i.e. spreading centers, trenches) can be modified by such processes (e.g. Hyndman & Peacock, 2003; Früh-Green *et al.*, 2004; Grevemeyer *et al.*, 2007; Frost & Beard, 2007; Cooperdock *et al.*, 2018). Most peridotite samples that have been dredged or drilled from the seafloor have experienced some degree of serpentinization (e.g. Bloomer & Fisher, 1987; Brandon *et al.*, 2000; Dick *et al.*, 2003; Bach *et al.*, 2004; Harvey *et al.*, 2006; Paulick *et al.*, 2006; Frisby *et al.*, 2016). Serpentinization can completely eradicate original protolith textures and can have a profound impact on some aspects of the chemistry of peridotites, (e.g. Snow & Dick, 1995; Mével, 2003; Bach *et al.*, 2004; Malvoisin, 2015; Bénard *et al.*, 2021) especially major element data (Fig. 1). The clear and profound effects of serpentinization on some elements (e.g. Sr, Ba) has been used as generalized evidence of its impact on bulk chemistry, even for some of the strongly compatible but low abundance elements, such as the highly siderophile elements (HSE: Os, Ir, Ru, Rh, Pt, Pd, Re, Au).

Despite some perceptions that serpentinization can lead to flawed interpretations in understanding the geochemistry of seafloor peridotites, there is limited quantitative evidence to support this idea for some elements, most especially for the HSE or Os isotopes. Previous studies specifically investigating these elements in peridotites spanning a wide range of seafloor alteration or serpentinization have been unable to provide systematic evidence for alteration effects (e.g. Snow & Reisberg, 1995; Alard *et al.*, 2005; Harvey *et al.*, 2006; Liu *et al.*, 2009; Day *et al.*, 2017b; Snortum & Day, 2020). Serpentinization processes have the potential to affect elemental abundances and isotopes in ultramafic rocks by the removal of elements (e.g. Mg or Ca), addition of elements, especially those enriched in seawater (e.g. B, Sr), and by volume increases that lead to dilutional effects on most elements. Understanding the impact of serpentinization on seafloor peridotite chemistry allows for further interpretation of important processes, including reactions occurring during serpentinization, and potentially enabling assessment of the delivery of water and other volatile species into the deep Earth during subduction (e.g. Kodolányi *et al.*, 2012; Guillot & Hattori, 2013). Even atmophile elements like Xe show strong evidence for deep lithospheric subduction (e.g. Mukhopadhyay & Parai, 2019). Consequently, addressing the behavior of elements within peridotites during serpentinization remains a critical goal for understanding mantle geochemistry.

The 1967 NOVA88D dredge by the *R/V Argo* at the Tonga Trench yielded some of the deepest and freshest recovered peridotites from the seafloor, as well as fully serpentinized peridotites (Fisher & Engel, 1969; Bloomer & Fisher, 1987; Bloomer *et al.*, 1996; Wright *et al.*, 2000; Birner *et al.*, 2017). The Tonga Trench is remarkable for being the second deepest trench on Earth and having a fast convergence rate of ~20 cm a year (Bevis *et al.*, 1995). Peridotites dredged from this setting have been interpreted to represent forearc peridotites sampled on the arc-side of the trench (Birner *et al.*, 2017). This study investigates harzburgite samples from the NOVA88D dredge to examine and quantify the role of serpentinization on HSE, and Os isotopes. Due to the freshness of some of these peridotites, it is possible to address the timing and extent of melt depletion, as well as to examine the petrogenesis and wider implications for oceanic mantle composition.

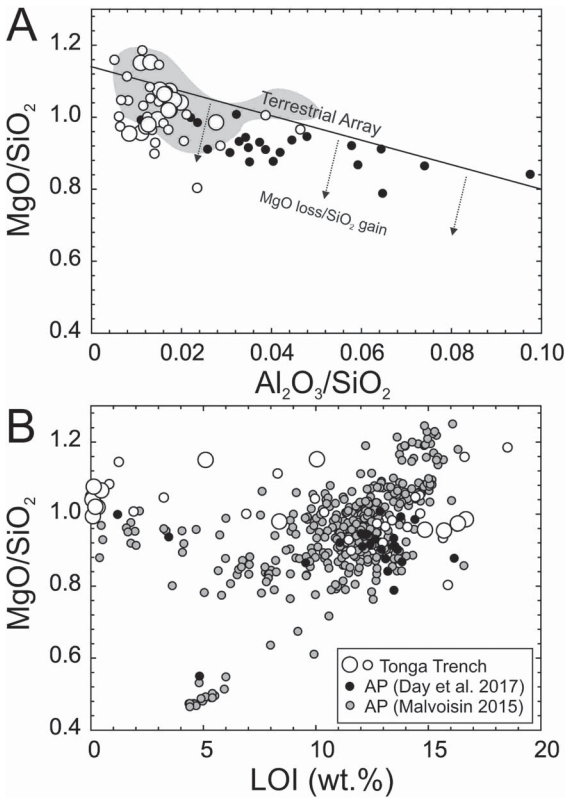

Fig. 1. Diagrams illustrating geochemical variations due to seafloor alteration and serpentinization in abyssal peridotites as a function of (A) Al_2O_3/SiO_2 vs. MgO/SiO_2 and (B) LOI vs. MgO/SiO_2. Shown are the compiled data from Malvoisin (2015), Day *et al.* (2017a), and for Tonga Trench peridotites from Birner *et al.* (2017). New results from Tonga Trench peridotites from this study are also shown as large unfilled circles.

SAMPLES

Visually fresh to completely serpentinized Tonga Trench peridotites, dredged during the 1967 NOVA expedition using the *R/V Argo*, were examined in this study (Table 1; Fig. 2). Samples came from dredge 88D, located at 20°25'S, 173°16'W, and between 9150 m and 9400 m water depth. Based on their observations during dredging operations, Fisher & Engel (1969) proposed that the samples were taken from the arc-side of the trench. These samples represent the deepest dredged suite of what have been interpreted to be forearc peridotites. In total, peridotites have been recovered in 14 dredges from nearly 1000 km of the Tonga Trench (Fisher & Engel, 1969; Bloomer & Fisher, 1987;

Table 1: Modal percentages of phases in Tonga Trench peridotites and LOI for sample powders

Sample	Olivine	Orthopyroxene	Clinopyroxene	Spinel	Veins	Serpentinite	LOI (%)
N88-A1*	79.0	19.9	0.1	0.90			
NOVA88D-1	68.2	30.6	1.0	0.20	-	0	0.10
NOVA88D-3	72.3	27.2	*Trace*	0.42	-	0	−0.07
NOVA88D-4	63.5	34.7	1.4	0.35	-	0	0.07
NOVA88D-6	72.0	26.0	1.5	0.50	-	0	0.46
NOVA88D-9	54.0	42.8	2.8	0.42	-	0	0.09
NOVA88D-10	68.6	31.1	*Trace*	0.29	-	0	0.13
NOVA88D-11	*81.6*	*17.5*	-	0.86	25.2	60	5.10
NOVA88D-12	*59.7*	*37.8*	-	2.44	-	97.5	14.9
NOVA88D-13	*63.3*	*36.5*	-	0.18	-	99.8	10.1
NOVA88D-15	*56.0*	*43.9*	-	0.15	2.5	99.8	16.3

Modal percentages of olivine and orthopyroxene estimated prior to serpentinization are given for serpentinized samples D-11, D-12, D-13 and D-15 using crystal morphologies preserved in samples. *Comparison sample, from same dredge, in Birner et al. (2017).

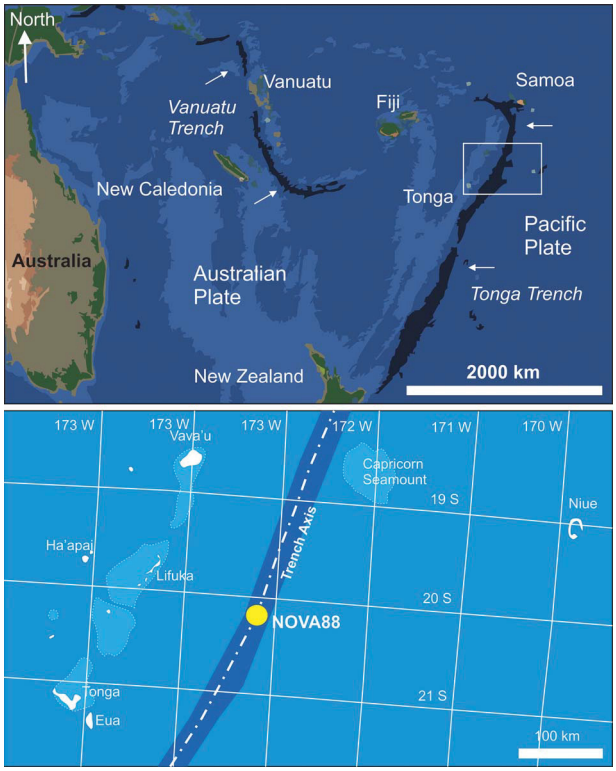

Fig. 2. Regional map (upper image) of the Tonga Trench with inset showing the location of NOVA 88 Dredge and study area (lower image). The Osborn trough is at 25°S.

Bloomer *et al.*, 1996; Wright *et al.*, 2000; Birner *et al.*, 2017), and are notable for their remarkable freshness in some instances (Birner *et al.*, 2016). Hand-samples between 20 g and 100 g were cut to form blocks using a precision saw. The cut edges were sanded using coarse grit corundum paper to remove sawn surfaces, and blocks were sonicated for ~5 minutes in distilled water before being dried. The cleaned blocks were then crushed to fragments of <5 mm using a ceramic alumina jaw crusher. A portion of the crush was then powdered to fine flour using an alumina shatter box.

METHODS

Mineral composition determinations and modal mineralogy

Mineral compositions and modal mineralogy were determined on polished thin sections. Petrographic analysis and determination of mineral modes was performed using a Nikon POL transmitted/reflected light microscope equipped with an imaging system for scaled-digitization of whole- or individual areas of thin-sections. Mineral modes were performed using methods developed previously for meteorites (Day *et al.*, 2006) and peridotite xenoliths (Traver, 2013). These studies have demonstrated reproducibility of better than 5% on samples with strong color contrasts, including fresh peridotites. Determination of modal analyses in serpentinized samples was possible where replacement appeared to be essentially static and original crystal morphologies were preserved.

Major element mineral compositions were obtained using a *Cameca* SX electron microprobe at the CAMPARIS facility in Paris (Universite Pierre et Marie Curie, Paris). Operating conditions were 15 keV accelerating voltage, a 5 μm beam diameter, with a 10 nA beam current, with counting times of 10–20 seconds (s) on background and peak for major elements. Minerals and pure oxides were used as standards for elemental calibration. Standards used were olivine for Mg and Si, pure magnetite for Fe, orthoclase for Al, diopside for Ca, albite for Na, pure chromite for Cr, manganese titanate for Mn and Ti, and vanadinite for V. Background and peak counting times used were 20–30 s and standard PAP correction procedures were used (Pouchou & Pichoir, 1987). Detection limits were < 0.03 wt. % for SiO_2, TiO_2, Al_2O_3, MgO, CaO, and Na_2O, <0.04 wt. % for V_2O_3 and Cr_2O_3, <0.05 wt. % for MnO, FeO, and NiO. Statistical uncertainties (2 standard deviations [SD]) resulting from counting statistics were 2% for FeO, MgO, CaO and SiO_2, 3% for Cr_2O_3, 5% for Al_2O_3, 15% for NiO, 20% for Na_2O and MnO, and 30% for TiO_2 and V_2O_3. The complete data set of these analyses is reported in *Table S1*.

Laser ablation inductively coupled plasma mass spectrometry (LA-ICP-MS) was used to analyze fresh silicate mineral phases using a *New Wave Research UP213* (213 nm) laser-ablation system coupled to a *ThermoScientific iCAP Qc* quadrupole inductively coupled plasma mass spectrometer (ICP-MS) at the *Scripps Isotope Geochemistry Laboratory (SIGL)*. Analyses were done using ~0.5 mm long rasters with a 100 μm beam diameter, a laser repetition rate of 5 Hz,

and a photon fluence of ~3 to 3.5 J/cm^2. Ablation analysis took place in a 3 cm^3 ablation cell. The cell was flushed with He-gas to enhance production and transport of fine aerosols and was mixed with an Ar carrier-gas flow of ~1 L/min, before reaching the torch. Each analysis consisted of ~60 s data collection. Backgrounds on the sample gas were collected for ~20 s, followed by ~40 s of laser ablation. Washout time between analyses was >120 s. Data were collected in time-resolved mode so effects of inclusions, mineral zoning and possible penetration of the laser beam to underlying phases could be evaluated. Plots of counts per second vs. time were examined for each analysis, and integration intervals for the gas background and the sample analysis were selected. Standardization was performed using the standard reference material glasses NIST 610, BCR-2 g and BHVO-2 g, yielding reproducibility of better than 8% (relative standard deviation [RSD]). Data were reduced using an in-house correction program and preferred concentrations of the standard reference materials were taken from the values from GeoReM. All data were initially corrected using NIST 610 with confirmation by constructing calibration curves from NIST 612, NIST 610, and BHVO-2 g, with Si as the normalizing element. The complete data set of these analyses is reported in *Table S2*.

Whole-rock major and trace element analysis

Major element compositions were measured by X-ray fluorescence (XRF) at Franklin and Marshall College using procedures outlined in Boyd & Mertzman (1987), with identical precision and accuracy to our previous work (Day *et al.*, 2017a). Whole-rock powders were measured for trace-element abundances at the *SIGL*. Samples were digested at 150°C in Optima grade concentrated HF (4 mL) and HNO_3 (1 mL) for >72 hours on a hotplate, with total analytical blanks, and terrestrial basalt standards. Samples were sequentially dried and taken up in concentrated HNO_3 to remove fluorides, followed by dilution and doping with a 1 µg/ml indium solution to monitor instrumental drift during analysis. Trace-element abundance analyses were done using a *ThermoScientific iCAP Qc* quadrupole ICP-MS in standard mode. Analyses were standardized vs. reference material BHVO-2 that was measured throughout the analytical run. In addition, reference materials were analyzed as 'unknowns' (BHVO-2, BIR-1, BCR-2 and HARZ-01) to assess matrix matching, external reproducibility, and accuracy. For trace-elements, reproducibility of the reference materials was better than 5% (RSD), except for B, W, Cs (all at 8% RSD) and Mo (17% RSD). The reproducibility is in line with standard reference material data reported previously for the laboratory (e.g. Day *et al.*, 2017a).

Rhenium-osmium and highly siderophile element abundance analysis

Osmium isotope and HSE abundance analyses were performed at *SIGL*. Homogenized 1 g powder aliquots of the NOVA dredge samples were digested in sealed borosilicate Carius tubes, or high-pressure asher (HPA) quartz digestion vessels, with isotopically enriched multi-element spikes (^{99}Ru, ^{106}Pd, ^{185}Re, ^{190}Os, ^{191}Ir, ^{194}Pt), and 11 mL of a 1:2 mixture of multiply Teflon distilled HCl and HNO_3 that was purged with H_2O_2 to remove Os. Samples were digested in Carius tubes to a maximum temperature of 270°C in an oven for 72 hours, and in HPA vessels for 6 hours at 320°C, and > 150 bar. Osmium was triply extracted from the acid using CCl_4 and then back extracted into HBr, prior to purification by micro-distillation, with the other HSE being recovered and purified from the residual solutions using anion exchange separation (Day *et al.*, 2016). Isotopic compositions of Os were measured in negative-ion mode on a *ThermoScientific* Triton thermal ionization mass spectrometer. Rhenium, Pd, Pt, Ru and Ir were measured using an *Cetac* Aridus II desolvating nebulizer coupled to a *ThermoScientific iCAP Qc* ICP-MS. Offline corrections for Os involved an oxide correction, an iterative fractionation correction using $^{192}Os/^{188}Os = 3.08271$, a ^{190}Os spike subtraction, and finally, an Os blank subtraction. Precision for $^{187}Os/^{188}Os$, determined by repeated measurement of the UMCP Johnson-Matthey standard was better than ±0.2% (2 SD; 0.11385 ± 17; $n = 6$). Measured Re, Ir, Pt, Pd and Ru isotopic ratios for sample solutions were corrected for mass fractionation using the deviation of the standard average run on the day over the natural ratio for the element. External reproducibility on HSE analyses using the iCAP Qc was better than 0.5% for 0.5 ng/g solutions and all reported values are blank corrected. The total procedural blanks ($n = 4$) run with the samples for Carius tubes had $^{187}Os/^{188}Os = 0.22 \pm 0.11$, with quantities (in picograms) of 0.9 [Re], 6 [Pd], 20 [Pt], 10 [Ru], 5 [Ir] and 0.72 [Os]. The total procedural blanks run using the HPA were 50% lower than these values with $^{187}Os/^{188}Os = 0.2$. All data are blank corrected, with the blanks representing between 0.1 and 46% (highest blank proportion in NOVA88D-17), 0.1 and 6%, <0.1 and 1%, <0.1 and 57%, 0.1 and 35% (highest blank proportions in NOVA88D-16), and < 0.1–5% of total measured Re, Pd, Pt, Ru, Ir and Os, respectively. The high blank estimates for Re in some peridotites reflect the low Re contents of these peridotites, rather than an elevated total procedural blank.

Harzburgite standard powder, HARZ-01 was run with samples three times during the analytical campaign, and concentrations and isotopic compositions for this standard reference material ([in ng/g with 2 SD uncertainties] 0.06 ± 0.01 [Re], 5.68 ± 0.35 [Pd], 7.8 ± 3.5 [Pt], 6.78 ± 1.55 [Ru], 4.30 ± 0.73 [Ir], 3.74 ± 0.78 [Os], $^{187}Re/^{188}Os = 0.075 \pm 0.022$, $^{187}Os/^{188}Os = 0.12503 \pm 0.00150$, are within uncertainty of a larger set of measurements made using both Carius tube and HPA digestion methods (Meisel & Horan, 2016; Day *et al.*, 2012). The harzburgite reference material, HARZ-01, is likely to reasonably approximate the Tonga Trench peridotite compositions, and the variations in HSE abundances reflect inhomogeneous distribution of sub-micron sized HSE-rich phases within the rock and sample powder. This so-called 'nugget effect' is well described in peridotite studies (e.g. Becker *et al.*, 2006 for a discussion). Consequently, the reproducibility on HSE abundances for the HARZ-01 reference material is likely to be a better approximation of reproducibility (6–45%) than the external analytical uncertainties.

RESULTS

Sixteen spinel-bearing harzburgite samples were measured that exhibited a visible range of fresh and altered mineralogical compositions in hand specimen. One associated seafloor basalt collected during the same dredge was also analyzed and is reported for completeness.

Modal mineralogy and composition of mineral phases

Tonga Trench peridotites are spinel harzburgites (54–82 modal % olivine; 17–43 modal % orthopyroxene; <0.1–2.8% clinopyroxene, and 0.2–2.4 modal % spinel), with serpentinization ranging from zero to 100%, with significant serpentinite veining within some samples (Table 1; Fig. 3). Magnetite grains occur within the serpentinized

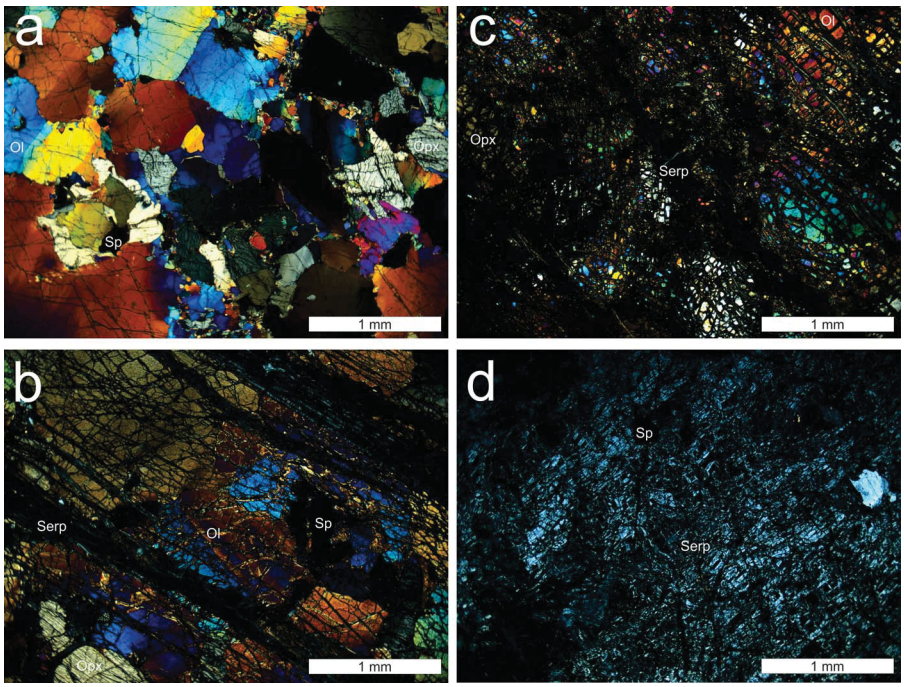

Fig. 3. Cross-polarized light photomicrographs of (a) NOVA88D-1 (0.1 wt.% LOI), (b) NOVA88D-11 (5.1 wt.% LOI), (c) NOVA88D-13 (10 wt.% LOI) and (d) NOVA88D-15 (16.3 wt.% LOI) illustrating the increasing degree of serpentinization (a is unserpentinized, d is almost completely serpentinized), corresponding to higher LOI.

material in samples that have experienced significant alteration (e.g. D-11, D-13). Texturally, the NOVA88D harzburgites can be defined as protogranular to porphyroclastic (after textural definitions by Mercier & Nicolas, 1975, and others), with evidence for strain within olivine, as well as exsolution lamellae within orthopyroxene, in the freshest samples (Fig. 4). Olivine and orthopyroxene grain sizes are typically in the ~1–4 mm diameter range but can exceed 5 mm in diameter. When present in samples, clinopyroxene grains are small (<0.5 mm in diameter). Spinel grains range in size from ~0.5 to 2 mm in diameter and are found as anhedral grains intergrown with orthopyroxene and small grains of olivine and clinopyroxene in some samples, as equant isolated grains, or as stringers within samples with evidence for strain. As with Tonga Trench peridotites examined by Birner *et al.* (2017), the spinel grains for samples of this study have sharp boundaries and do not have sieve textures or compositional zonation in backscattered electron images. Evidence for later melt veins, plagioclase or amphibole is absent in the peridotites.

Thirty-four individual olivine grains from eight samples gave a restricted range in forsterite contents (90.1–91.9), with low CaO (<0.05 wt.%) and NiO of 0.40 ± 0.05 wt.% (*Table S1*). Seventy-seven orthopyroxene grains measured from the studied samples have a relatively homogeneous composition ($Wo_{2.1\pm1.8}En_{89.7\pm1.6}Fs_{8.2\pm0.4}$), with 1.6 ± 0.2 wt.% Al_2O_3 and 0.60 ± 0.06 wt.% Cr_2O_3. Twenty-one clinopyroxene grains from six samples are also relatively homogeneous, close to diopside ($Wo_{48.2\pm2.3}En_{49.1\pm2.3}Fs_{2.7\pm0.3}$), with low Na_2O (0.11 ± 0.03 wt.%), 1.7 ± 0.3 wt.% Al_2O_3, and 0.8 ± 0.1 wt.% Cr_2O_3. Cr-spinel compositions have Cr-numbers ranging from 53 to 76 and Mg-numbers from 46 to 57, making them some of the most depleted spinel compositions from any oceanic peridotites worldwide (Fig. 5). These compositions for mineral grains are broadly similar to those reported by Birner *et al.* (2017) for Tonga Trench peridotites. The extreme depletion from Cr- and Mg-numbers in spinel would be consistent with 20 ± 1% partial melt extraction using the modified method of Hellebrand *et al.* (2001), indicating that Tonga Trench peridotites are more depleted than typical residual abyssal peridotites (Warren, 2016).

Mineral trace-element abundances are provided in Table S2 and Figs 6 and 7. In general, rare earth element (REE) abundances are highest in clinopyroxene relative to orthopyroxene or olivine (Fig. 6), as expected from general trace element partitioning behavior in these phases. However, mineral phases analyzed for REE abundances in Tonga Trench peridotites are all systematically depleted relative to depleted mid-ocean ridge basalt mantle (DMM) (Fig. 7). Tonga Trench peridotite clinopyroxene and orthopyroxene grains have lower absolute abundances of the REE than 'average DMM' compositions (Workman & Hart, 2005) and are broadly similar to some residual Gakkel Ridge abyssal peridotites (e.g. D'Errico *et al.*, 2016) and to data obtained for a selection of Tonga Trench peridotites by Birner *et al.* (2017). When plotted as primitive mantle normalized multi-incompatible trace element diagrams, orthopyroxenes have a broadly 'U-shaped' pattern, with pronounced relative enrichment in Pb with all elements being relatively depleted from 0.01 to 0.1 × PM (Fig. 6). Orthopyroxene grains have PM normalized (N) La/Yb of 0.016 ± 0.033, Dy/Yb_N of 0.86 ± 0.09, Zr/Hf_N of 1.06 ± 0.61 and Nb/Ta_N of 1.94 ± 0.63 ($n = 36$). Clinopyroxene grains have a more 'sinusoidal' pattern at ~0.1 × PM, with relative enrichments in the light REE (e.g. La, Ce), relative to the heavy REE (e.g. Tm, Yb). In one case (NOVA 88D-2-2b CPX), the analysis yielded anomalously high Zr, Hf, Th and U indicating partial ablation of an HFSE-rich phase or fraction during clinopyroxene analysis. The clinopyroxene grains have La/Yb_N of 0.19 ± 0.12, Dy/Yb_N of 0.30 ± 0.17, Zr/Hf_N of 2.3 ± 2.6 and Nb/Ta_N of 3.8 ± 1.9 ($n = 19$). Olivine grains ($n = 21$) have low trace element abundances (typically <0.01 × PM values), with partial enrichments in U and Pb, with

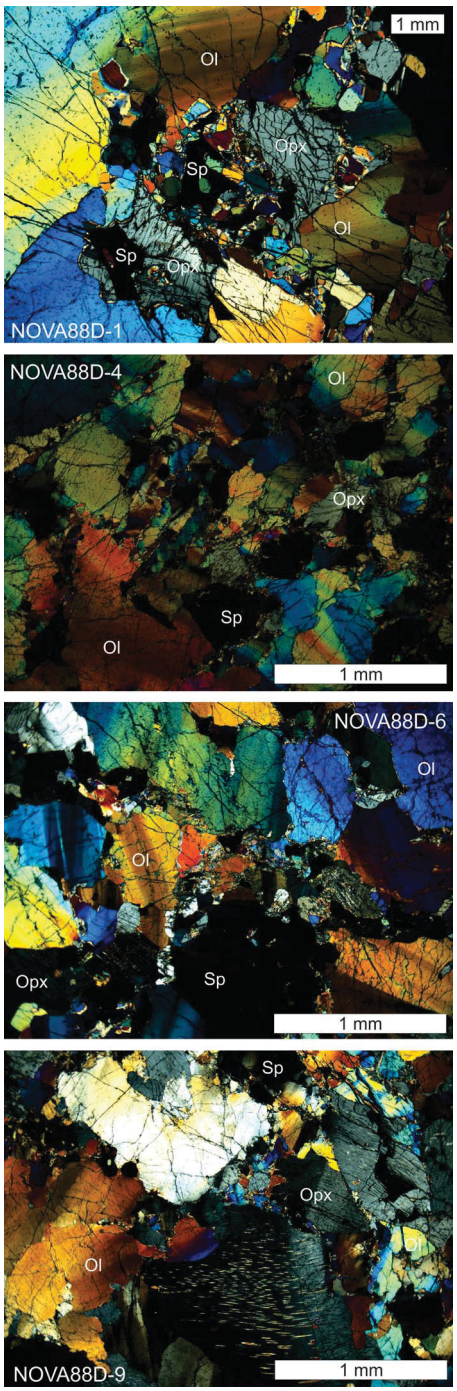

Fig. 4. Cross-polarized light photomicrographs of NOVA88D-1, NOVA88D-4, NOVA88D-6 and NOVA88D-9 illustrating textural and mineralogical features in the fresh harzburgites and evidence for strain in olivine and orthopyroxene, as well as exsolution in NOVA88D-9 orthopyroxene. Abbreviations: Ol = olivine; Opx = orthopyroxene; Sp = spinel.

a subset of olivine grains with light REE enrichment. The light REE enriched olivine grains have La/Yb_N of 3.9 ± 0.9, Zr/Hf_N of 2.1 ± 1.3 and Nb/Ta_N of 0.15 ± 0.21. The 'normal' olivine grains have La/Yb_N of 0.24 ± 0.31, Dy/Yb_N of 0.17 ± 0.25, Zr/Hf_N of 1.03 ± 0.69 and Nb/Ta_N of 0.47 ± 0.41.

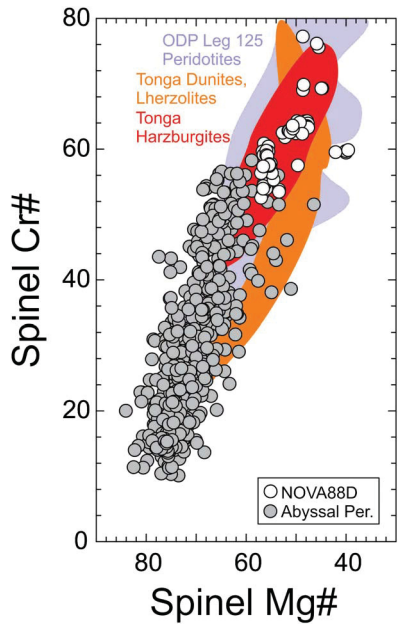

Fig. 5. Spinel magnesium-number (Mg#) vs. chromium-number (Cr#) for Tonga Trench peridotites (unfilled circles) vs. the residual abyssal peridotite data set of Warren (2016) (grey circles) and the field of spinel data for ODP Leg 125 peridotites from the Izu-Bonin Marianas forearc (Parkinson & Pearce, 1998). Also shown are data fields for Tonga Trench harzburgites, dunites and lherzolites from Birner *et al.* (2017). Tonga Trench peridotites have been highly melt-depleted relative to the global suite of residual abyssal peridotites.

Bulk-rock major and trace element abundances

Tonga Trench peridotites have highly depleted compositions, with MgO contents from 43.2 to 47.5 wt.%, low Al_2O_3 (0.4 to 0.8 wt.%) and CaO (0.12 to 0.8 wt.%), with high Ni and Cr contents (2000 to 2450 μg/g, and 2300 to 3050 μg/g, respectively) (Table 3). An outlier in the data set is sample NOVA88D-5, which has higher Al_2O_3 (1.2 wt.%), K_2O and P_2O_5 than the other studied peridotites; due to these differences, this sample will be treated separately from others. Loss on ignition (LOI) ranges from negative values (likely due to oxidation of Fe^{2+} to Fe^{3+} during the process) to 16.7 wt.%, consistent with petrological evidence for fresh to highly serpentinized peridotites. These results are consistent with previously presented data for bulk rock compositions of Tonga Trench peridotites (Birner *et al.*, 2017).

Minor- and trace-element compositions in the peridotite bulk rocks are characterized by high compatible element abundances (e.g. Ni >2000 μg/g, Cr, Co), and low incompatible element abundances (e.g. Li, P, Sc, Ti, Cu, Zn). The samples are generally more depleted than residual abyssal peridotites from the Gakkel Ridge, having low REE abundances (Fig. 8). The exception to this rule is the similarity in incompatible trace element composition in NOVA88D-5 compared with some of the Gakkel Ridge abyssal peridotites (Day *et al.*, 2017a), and the pervasively high Ga contents in all the Tonga Trench peridotites, suggesting anomalous behavior for this element. Fluid mobile elements, including Rb, Ba, Cs, U, Pb and Sr are highly variable in the peridotites, implying varying degrees of fluid–rock interaction. Most minor- and trace-elements do not vary with LOI, but several of the fluid mobile elements are correlated with LOI (e.g. Na_2O, B, Sr have R^2 values of 0.94, 0.85, and 0.74, respectively; Figs 9 and 10. Note: R^2 values are reported here to define general trends in data. It should be recognized that the largely bimodal nature of the sample set [i.e.

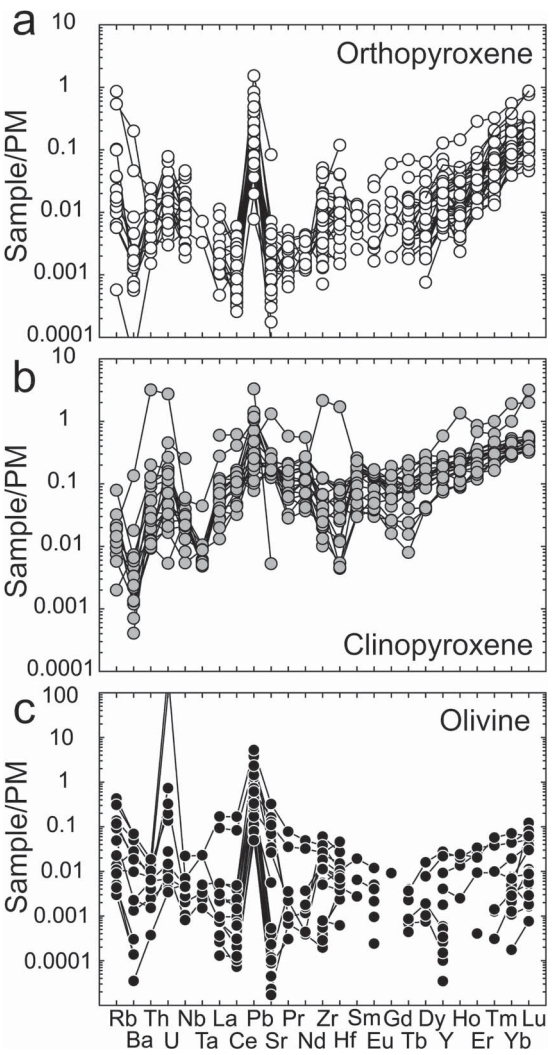

Fig. 6. Primitive mantle (PM) normalized incompatible trace element diagrams for (a) orthopyroxene, (b) clinopyroxene, and (c) olivine in Tonga Trench peridotites determined by LA-ICP-MS. Primitive mantle normalization from McDonough & Sun (1995).

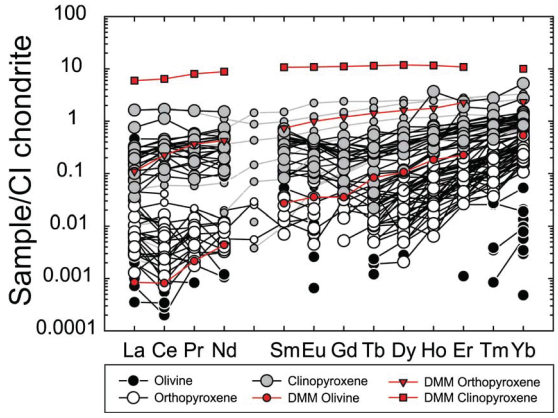

Fig. 7. CI-chondrite normalized REE diagram for orthopyroxene, clinopyroxene and olivine in Tonga Trench peridotites relative to mean compositions of these minerals in the DMM. Smaller symbols are data for Tonga Trench peridotites from Birner *et al.* (2017). DMM data from Workman & Hart (2005), and CI-chondrite normalization from McDonough & Sun (1995).

fresh vs. serpentinized peridotites] will inevitably lead to correlations or anticorrelations in some comparisons).

REE compositions are consistent with strong depletions for both the light REE (LREE) and the heavy REE (HREE), with strong concave up profiles. There are two patterns that most samples fall within, with either a decrease in abundance from the LREE to the middle REE (MREE), and a subsequent increase to the HREE (LREE > MREE < HREE), or a gradual increase from LREE to MREE and a sharper increase from MREE to HREE (LREE ≤ MREE < HREE). The one exception to this is NOVA88D-5, which shows much higher abundances of the MREE and HREE than the rest of the samples and follows a concave down trend.

The lava sample (NOVA88D-16) dredged with the peridotite samples is a basanite composition with high total alkalis ($Na_2O + K_2O = \sim 7.3$ wt.%) and 9.4 wt.% MgO and a high LOI (8.6 wt.%). The lava is characterized by relatively low compatible trace element abundances relative to the peridotites, with much higher incompatible trace element compositions and an incompatible trace element enriched signature (Fig. 8).

Highly siderophile element abundances and $^{187}Os/^{188}Os$ ratios

Peridotites from the Tonga Trench have variable absolute and relative abundances of the HSE relative to primitive mantle compositions (Becker *et al.*, 2006; Day *et al.*, 2017a) and can be highly depleted in Re and Pd, and even Ir and Os, in some samples (Table 4; Fig. 11). Replicate analyses of six samples were accomplished using Carius tube and HPA digestion, with any differences reflecting the previously noted 'nugget effect' of uneven distribution of the HSE within peridotite samples. The most fractionated patterns for the peridotites occur in NOVA88D-5 (16.7 wt.% LOI), NOVA88D-15 (16.3 wt.% LOI) and NOVA88D-11 (5.1 wt.% LOI), but less fractionated patterns, relative to the primitive mantle also occur in peridotites with high LOI (e.g. NOVA88D-12). Rhenium abundances are highest in the most strongly serpentinized samples and Pt and Pd abundances are generally lowest in these rocks, with no relation between abundance and LOI for Os, Ir or Ru. Nonetheless, Os/Ir and Ru/Ir are generally higher in serpentinized than fresh peridotites, but these samples also have the highest estimated degrees of melt depletion (Fig. 12). Compared with abyssal peridotites from the Indian, Atlantic and Arctic oceans (Day *et al.*, 2017a), Tonga Trench peridotites are generally more depleted in Re and can have higher absolute Os, Ir, Ru and Pt abundances. The single lava sample that we measured is depleted in Os, Ir and Ru and has higher Re and Pd, consistent with typical basaltic partial melts (Day, 2013).

Isotopic ratios for $^{187}Re/^{188}Os$ and $^{187}Os/^{188}Os$ for the peridotites range from 0.006 to 9.6 and 0.1192 to 0.1432, respectively with an average $^{187}Os/^{188}Os$ ratio of 0.1265 ± 0.098 (2 SD; $n = 16$). NOVA88D-5 is the most radiogenic peridotite sample ($^{187}Os/^{188}Os = 0.1368$–$0.1432$). Given the geochemical distinction of this sample, noted above, its removal from the data set gives an average $^{187}Os/^{188}Os$ ratio of 0.1252 ± 0.0050 (2 SD). The most unradiogenic sample is NOVA88D-7 with $^{187}Os/^{188}Os$ of 0.1192 with a Re depletion age (T_{RD}) of ~1.5 Ga. On a $^{187}Re/^{188}Os$-$^{187}Os/^{188}Os$ plot some samples, including the lava (D-16) and D-5 lie along a ~125 Ma isochron (Fig. 13). This age is older than the interpreted age of the subducting seafloor in this region (P. Castillo & J. Gee, Pers. Comm.), which is held to be associated with the formation of the ~90 Ma Osborn Trough (Downey *et al.*, 2007). This inferred age

Table 2: Mineral compositions and olivine-spinel-orthopyroxene thermo-oxybarometry

	Olivine		Spinel			%	Orthopyroxene				Clinopyroxene				T (Ol-Sp)[a]		T (2 Px)[a]		T (Ca Opx)[a]		fO_2[b]	
	n	Forsterite	*n*	Cr#	Mg#	Melt Dep.	*n*	Wo	En	Fs	*n*	Wo	En	Fs	°C	± 2 SD[c]	°C	± 2 SD[c]	°C	± 2 SD[c]	Δlog FMQ	± 2 SD[d]
NOVA88D-1	*6*	0.913	*11*	0.598	0.56	19.7	*5*	2.0	90.1	7.9	*5*	49.1	48.2	2.7	879	28	842	95	1062	192	−0.5	0.5
NOVA88D-2	*4*	0.915					*4*	1.5	90.4	8.1	*4*	45.7	51.9	2.5					987	129		
NOVA88D-3							*6*	2.1	90.1	7.7									1081	292		
NOVA88D-4	*4*	0.913	*10*	0.540	0.557	18.7	*6*	1.5	90.2	8.3	*2*	49.4	48.0	2.6	832	40	709	38	1000	170	−0.1	0.5
NOVA88D-5			*1*	0.772	0.486	22																
NOVA88D-6	*7*	0.911	*6*	0.592	0.419	19.6	*4*	2.4	89.2	8.4					713	85			1116	86	−0.6	0.5
NOVA88D-7			*2*	0.622	0.524	20	*10*	2.1	89.9	8.0	*4*	48.5	48.7	2.8			738	136	1035	327		
NOVA88D-8							*6*	1.3	90.2	8.4									965	340		
NOVA88D-9	*3*	0.903	*12*	0.633	0.485	20	*7*	2.1	89.2	8.7	*5*	48.7	48.4	2.9	847	60	833	266	943	211	−0.5	0.5
NOVA88D-10	*2*	0.911	*9*	0.569	0.557	19.2	*8*	1.7	90.0	8.3					866	68			1024	92	−0.3	0.5
NOVA88D-11	*6*	0.910	*11*	0.631	0.503	20.3	*9*	1.3	90.5	8.3	*2*	48.9	48.4	2.6	844	64	835	206	958	291	−0.4	0.5
NOVA88D-12			*4*	0.694	0.467	21.2	*8*	3.2	88.9	8.0									1060	730		
NOVA88D-14			*2*	0.759	0.457	22.2																
NOVA88D-17	*2*	0.919					*1*	5.2	87.7	7.1												

	T (Ol-Sp)[a] °C	± 2 SD[c]	T (2 Px)[a] °C	± 2 SD[c]	T (Ca Opx)[a] °C	± 2 SD[c]	fO_2[b] Δlog FMQ	± 2 SD[d]
Average for all NOVA 88D estimates (all estimates assume presure of 0.6 Gpa, consistent with Birner et al., 2017)	**830**	**120**	**791**	**126**	**1021**	**111**	**−0.4**	**0.4**
Average Tonga Trench (Birner et al., 2017)	874	73					0.1	1.6
Abyssal Peridotite (Udinsev Ridge WEST-03-MV12; Paquet et al., 2021; n = 6)	840	47	1210	53	1286	127	0.5	0.4
Abyssal Peridotite (Udinsev Ridge WEST-03-MV13; Paquet et al., 2021; n = 4)	827	50	1117	221	1221	54	−2.9	2.8
Average Abyssal Peridotite (Bryndzia and Wood, 1990)	*950*	*50*					*0.0*	*1.6*
Average Conical Seamount Harzburgite (Parkinson & Pearce, 1998)	*856*						*−0.1*	
Average Torishima Forearc Seamount Harzburgite (Parkinson & Pearce, 1998)	*854*						*1.2*	
Average South Sandwich Forearc (Pearce et al., 2000)	*842*						*1.1*	
Average Subduction Xenoliths (Parkinson et al., 2003)	*1052*	*190*					*1.6*	*1.3*

[a]Thermometers after Brey & Kohler (1990) and Li *et al.* (1995)
[b]Calculation of fO_2 using the method of Davis *et al.* (2017)
[c]Two standard deviation calculated from 2 standard deviations of electronmicroprobe measurements for each oxide, or external analytical uncertianties, whichever was larger.
[d]Two standard deviation of the uncertainty from calculations using the three different themometers at 0.6 Gpa (if relevant to the thermometer).

Table 3: Bulk-rock major and trace element compositions for Tonga Trench peridotites and a single basalt

Sample	NOVA 88D-1	NOVA 88D-2	NOVA 88D-3	NOVA 88D-4	NOVA 88D-5	NOVA 88D-6	NOVA 88D-7	NOVA 88D-8	NOVA 88D-9	NOVA 88D-10	NOVA 88D-11	NOVA 88D-12	NOVA 88D-13	NOVA 88D-14	NOVA 88D-15	NOVA 88D-17	NOVA 88D-16
Type	Peridotite	Peridotite	Peridotite	Peridotite	Peridotite	Peridotite	Peridotite	Peridotite	Peridotite	Peridotite	Peridotite	Peridotite	Peridotite	Peridotite	Peridotite	Peridotite	Basalt
Wt.%																	
SiO_2	43.31	42.62	43.00	43.36	44.44	42.67	44.12	44.73	44.33	42.77	41.12	45.15	41.23	45.26	44.38	43.79	48.41
TiO_2	<0.01	<0.01	<0.01	<0.01	0.01	<0.01	<0.01	<0.01	<0.01	<0.01	<0.01	<0.01	<0.01	<0.01	<0.01	<0.01	2.98
Al_2O_3	0.80	0.74	0.70	0.86	1.23	0.70	0.76	0.57	0.65	0.65	0.45	0.50	0.54	0.38	0.54	0.76	15.68
Fe_2O_3T	8.5	8.97	8.8	8.85	8.87	9.21	8.45	8.75	8.87	8.83	9.1	9.3	9.06	9.29	10.04	8.66	10.09
MnO	0.118	0.117	0.130	0.120	0.148	0.160	0.118	0.143	0.130	0.119	0.122	0.105	0.123	0.107	0.129	0.124	0.135
MgO	45.36	45.73	45.72	45.11	43.79	45.47	44.96	43.80	44.07	46.02	47.31	43.18	47.51	43.18	43.23	44.67	9.39
CaO	0.70	0.50	0.49	0.72	0.12	0.76	0.69	0.54	0.82	0.61	0.38	0.39	0.22	0.12	0.15	0.74	4.65
Na_2O	0.02	0.02	0.01	0.01	0.16	0.05	0.02	0.09	0.02	0.01	0.05	0.12	0.07	0.13	0.15	0.02	4.25
K_2O	<0.001	<0.001	<0.001	0.001	0.018	<0.001	<0.001	0.007	<0.001	<0.001	0.002	0.013	0.005	0.011	0.006	<0.001	3.085
P_2O_5	0.002	0.002	0.003	0.003	0.006	0.002	0.003	0.002	0.002	0.004	0.004	0.004	0.004	0.003	0.003	0.003	0.894
Total	98.8	98.7	98.9	99.0	98.8	99.0	99.1	98.6	98.9	99.0	98.6	98.8	98.8	98.5	98.6	98.8	99.6
LOI	0.10	−0.09	−0.07	0.07	16.67	0.46	0.30	8.38	0.09	0.13	5.10	14.85	10.05	15.70	16.31	0.20	8.63
μg/g																	
Li	0.1	0.25	0.28	0.16	1.38	0.2	0.26	0.23	0.38	0.22	0.2	0.64	0.17	0.47	0.26	0.19	80.88
B	0.8	0.55	0.59	1.04	52.18	0.9	0.92	8.6	0.66	0.57	2.8	28.54	6.86	40.75	28.13	1.21	10.38
P	71.5	66.84	72.35	71.09	84.42	69.4	76.61	68.3	66.89	70.65	65.3	79.4	73.41	74.12	72.82	71.32	3527.83
Sc	4.9	4.7	4.6	4.8	7.6	4.1	5.1	4.3	6.5	5.2	2.6	4.2	2.5	4.8	4	5.4	17.3
Ti	9.7	24.3	21.2	12.4	43.9	10.3	65	12.5	23.8	9.4	7.6	11.7	18.8	10.9	8	25.8	16285.2
V	32.2	27.3	26.7	33.1	97	32.8	29.1	28.6	32.6	26.9	21.4	27.2	16.8	29.9	22.6	30.9	133.9
Cr	3000	3053	3052	2645	1247	3271	2570	2496	2587	2091	2793	2929	2110	3150	2324	2616	246
Mn	728.2	763.3	763.1	732.2	856.1	732.8	742.1	886.4	810.9	755.5	705.6	641.2	758.4	666.6	791.2	781	1055.1
Co	104.0	108.9	110.9	103.9	86.6	106.4	99.9	92.0	101.6	106.7	104.6	105.5	107.1	112.1	112.8	104.4	35.3
Ni	2321	2385	2451	2294	1717	2344	2208	2004	2095	2364	2405	2181	2361	2324	2426	2228	211
Cu	2.2	1.8	6.8	2.3	27.6	3.8	4.5	1.4	4.1	3.3	5.3	4.5	2	2.8	3.6	3.7	28.4
Zn	45.8	45.6	44	40.7	30.2	44.9	41.1	39.5	40.7	41.1	42.9	46.2	43.5	44.4	48.3	41.5	110.2
Ga	0.5739	0.6025	0.5683	0.5883	1.5438	0.5662	0.653	0.4975	0.529	0.4602	0.3726	0.7773	0.4115	0.5838	2.9913	0.5966	15.72
Ge	0.8410	0.844	0.8338	0.7884	0.834	0.8163	0.8106	0.8748	0.8264	0.8273	0.7990	0.7517	0.754	0.7672	0.7847	0.774	1.37
Rb	0.0113	0.0068	0.0051	0.0073	0.1561	0.0244	0.0565	0.1496	0.0171	0.0124	0.0390	0.2267	0.0616	0.1056	0.0637	0.05	50.43
Sr	0.2569	0.2155	0.2771	0.5581	6.3414	0.2962	0.3869	1.2371	0.3578	0.2469	0.6211	8.6076	0.9534	4.5294	6.4469	0.4805	264.68
Y	0.0121	0.0198	0.0164	0.014	1.2033	0.0092	0.0583	0.015	0.038	0.0094	0.0053	0.0143	0.013	0.0179	0.0052	0.0523	35.71
Zr	0.0555	0.0561	0.0543	0.0533	4.1378	0.0343	0.154	0.0302	0.0475	0.032	0.0204	0.0468	0.0331	0.0263	0.0238	0.2424	313.21
Nb	0.0073	0.0053	0.0052	0.0052	0.0079	0.0049	0.022	0.0049	0.0042	0.0038	0.0037	0.0081	0.0039	0.0052	0.0039	0.0312	56.62
Mo	0.1855	0.1157	0.0998	0.0849	0.3864	0.0724	0.0562	0.1294	0.0476	0.046	0.0575	0.1462	0.0682	0.1199	0.0705	0.0404	1.06
Cs	0.0036	0.0013	0.0012	0.002	0.0165	0.0116	0.0225	0.0293	0.0034	0.0035	0.0051	0.0425	0.0063	0.0147	0.0179	0.0042	1.45
Ba	1.5927	0.6959	0.1665	0.3552	4.1728	0.2220	0.6964	0.2754	0.2666	0.1331	0.3537	1.4046	0.3766	0.5578	0.9981	0.4055	726.55
La	0.0036	0.0021	0.002	0.0023	0.0115	0.0013	0.0111	0.0023	0.002	0.0017	0.0006	0.0067	0.0012	0.01	0.0072	0.0179	37.10

(Continued)

Table 3: Continued

Sample	NOVA 88D-1	NOVA 88D-2	NOVA 88D-3	NOVA 88D-4	NOVA 88D-5	NOVA 88D-6	NOVA 88D-7	NOVA 88D-8	NOVA 88D-9	NOVA 88D-10	NOVA 88D-11	NOVA 88D-12	NOVA 88D-13	NOVA 88D-14	NOVA 88D-15	NOVA 88D-17	NOVA 88D-16
Type	Peridotite	Peridotite	Peridotite	Peridotite	Peridotite	Peridotite	Peridotite	Peridotite	Peridotite	Peridotite	Peridotite	Peridotite	Peridotite	Peridotite	Peridotite	Peridotite	Basalt
Ce	0.0087	0.0055	0.0049	0.0051	0.0347	0.0027	0.0231	0.0039	0.005	0.0041	0.0015	0.0139	0.0028	0.0237	0.0075	0.0372	78.18
Pr	0.0012	0.0008	0.0007	0.0006	0.0057	0.0003	0.003	0.0004	0.0007	0.0005	0.0002	0.0017	0.0003	0.0024	0.0006	0.0044	9.75
Nd	0.0048	0.0044	0.0035	0.0023	0.0344	0.0014	0.0136	0.0016	0.0032	0.0017	0.0008	0.0077	0.0011	0.0108	0.0024	0.0181	40.45
Sm	0.0011	0.0013	0.0013	0.0006	0.0222	0.0003	0.0035	0.0005	0.0012	0.0003	0.0003	0.0017	0.0004	0.0019	0.0005	0.0041	9.07
Eu	0.0003	0.0003	0.0003	0.0001	0.0116	0.0001	0.0012	0.0001	0.0005	0.0001	0.0001	0.0006	0.0001	0.0005	0.0002	0.0013	3.06
Gd	0.0011	0.0012	0.001	0.0005	0.059	0.0003	0.0041	0.0007	0.0025	0.0004	0.0005	0.0019	0.0002	0.0021	0.0005	0.0043	9.28
Tb	0.0002	0.0002	0.0002	0.0001	0.0161	0.0001	0.0009	0.0002	0.0006	0.0001	0.0001	0.0003	0.0001	0.0003	0.0001	0.0008	1.32
Dy	0.0015	0.0021	0.002	0.0011	0.1416	0.0007	0.0083	0.0018	0.0059	0.0008	0.0009	0.002	0.0013	0.0021	0.0006	0.006	7.56
Ho	0.0006	0.0009	0.0007	0.0006	0.0347	0.0004	0.0024	0.0007	0.0018	0.0005	0.0003	0.0006	0.0006	0.0006	0.0002	0.0018	1.42
Er	0.0031	0.0048	0.0041	0.0038	0.1195	0.0027	0.0104	0.0035	0.0075	0.0027	0.0015	0.0025	0.0033	0.0027	0.0014	0.0074	3.79
Tm	0.0009	0.0012	0.001	0.0011	0.0223	0.0008	0.002	0.001	0.0016	0.0009	0.0004	0.0007	0.0009	0.0007	0.0004	0.0014	0.50
Yb	0.0092	0.0121	0.0108	0.0118	0.186	0.0089	0.0181	0.011	0.0147	0.0097	0.0047	0.0081	0.0084	0.0072	0.0058	0.0138	3.09
Lu	0.0022	0.0027	0.0024	0.0027	0.0349	0.0022	0.0036	0.0026	0.003	0.0023	0.0012	0.002	0.002	0.0017	0.0016	0.0029	0.44
Hf	0.0016	0.0015	0.0015	0.0018	0.0385	0.0011	0.0052	0.0008	0.0018	0.0011	0.0007	0.0013	0.001	0.0008	0.0006	0.0036	7.50
Ta	0.0015	0.0011	0.0012	0.001	0.0012	0.0009	0.0021	0.0009	0.0009	0.0009	0.0009	0.001	0.0009	0.0008	0.0007	0.002	3.88
W	0.0035	0.0028	0.0044	0.0045	0.0925	0.0167	0.0058	0.0475	0.0051	0.0038	0.0162	0.0425	0.0308	0.2185	0.0188	0.0056	0.17
Pb	0.0515	0.0572	0.0251	0.0279	0.3036	0.0297	0.0203	0.0699	0.0148	0.0694	0.0122	0.048	0.0768	0.1011	0.0864	0.0511	2.18
Th	0.0001				0.0002		0.0005	0.0001						0.0001	0.0001	0.0030	4.25
U	0.0052	0.0065	0.0113	0.0190	0.2732	0.0086	0.0144	0.0107	0.0059	0.0089	0.0034	0.2023	0.0061	0.2655	0.0076	0.0089	1.01

Table 4: HSE abundances (in ng/g) and $^{187}Os/^{188}Os$, with Al_2O_3, LOI and spinel modes, for Tonga Trench peridotites

Sample ID	Lithology	Method	Al_2O_3 (wt.%)	LOI (%)	Melt Sp (%)	Re	Pd	Pt	Ru	Ir	Os	$^{187}Re/^{188}Os$	2σ	$^{187}Os/^{188}Os$	2σ	γOs_{90Ma}[a]	T_{RD}[b]
NOVA88D-1	Harzburgite	Carius Tube	0.80	0.10	19.7	0.011	2.52	7.20	6.00	3.28	3.01	0.0177	0.0003	0.12865	0.00010	1.3	138
Repeat		HPA				0.062	1.95	11.00	3.15	1.88	2.58	0.1150	0.0017	0.12784	0.00011	0.5	273
NOVA88D-2	Harzburgite	Carius Tube	0.74	−0.09		0.009	1.29	3.10	9.30	3.96	6.48	0.0064	0.0001	0.12603	0.00008	−0.8	504
NOVA88D-3	Harzburgite	Carius Tube	0.70	−0.07		0.055	12.2	5.93	6.17	3.43	2.99	0.0881	0.0013	0.12419	0.00009	−2.3	779
NOVA88D-4	Harzburgite	Carius Tube	0.86	0.07	18.7	0.031	4.24	7.27	6.96	3.39	3.06	0.0484	0.0007	0.12472	0.00010	−1.8	697
NOVA88D-5	Harzburgite	Carius Tube	1.23	16.67	22	1.74	1.67	7.30	1.11	0.680	1.63	5.138	0.077	0.13677	0.00012	1.6	76
Repeat		HPA				1.86	1.81	7.44	0.87	0.426	0.93	9.62	0.14	0.14319	0.00026	1.4	120
NOVA88D-6	Harzburgite	Carius Tube	0.70	0.46	19.6	0.084	6.22	8.92	7.29	4.17	3.95	0.1020	0.0015	0.12660	0.00008	−0.4	444
NOVA88D-7	Harzburgite	Carius Tube	0.76	0.30	20.0	0.030	3.14	14.6	11.9	8.41	6.57	0.0217	0.0003	0.11929	0.00008	−6.1	1446
Repeat		HPA				0.275	2.78	9.5	2.9	5.20	3.09	0.4282	0.0064	0.11915	0.00015	−6.7	1549
NOVA88D-8	Harzburgite	Carius Tube	0.57	8.38		0.074	8.71	5.14	16.7	5.48	8.52	0.0420	0.0006	0.12524	0.00012	−1.4	622
Repeat		HPA				0.300	7.49	7.03	6.0	2.28	3.89	0.3719	0.0056	0.12483	0.00012	−2.1	749
NOVA88D-9	Harzburgite	Carius Tube	0.65	0.09	20.0	0.019	8.62	37.2	5.07	4.97	4.12	0.0221	0.0003	0.12565	0.00009	−1.1	561
NOVA88D-10	Harzburgite	Carius Tube	0.65	0.13	19.2	0.066	8.07	5.72	6.63	3.35	2.85	0.1119	0.0017	0.12446	0.00010	−2.1	746
NOVA88D-11	Harzburgite	Carius Tube	0.45	5.10	20.3	0.013	0.960	2.61	3.20	0.531	1.62	0.0373	0.0006	0.12667	0.00014	−0.3	421
Repeat		Carius Tube									3.08			0.12627	0.00008	−0.6	469
Repeat		HPA				0.330	1.194	8.47	3.57	0.925	1.69	0.943	0.014	0.12758	0.00023	−0.6	484
NOVA88D-12	Harzburgite	Carius Tube	0.50	14.85	21.2	0.180	1.77	8.23	7.28	3.48	6.64	0.1310	0.0020	0.12568	0.00009	−1.2	580
NOVA88D-13	Harzburgite	Carius Tube	0.54	10.05		0.049	0.949	2.16	11.0	3.11	10.4	0.0228	0.0003	0.12279	0.00009	−3.3	960
NOVA88D-14	Harzburgite	Carius Tube	0.38	15.70	22.2	0.111	1.65	10.8	9.40	4.27	4.75	0.1123	0.0017	0.12515	0.00015	−1.6	650
NOVA88D-15	Harzburgite	Carius Tube	0.54	16.31		0.030	0.842	5.77	1.76	0.13	0.168	0.864	0.013	0.12463	0.00035	−2.9	880
Repeat		HPA				0.246	0.903	9.13	1.30	0.13	0.206	5.753	0.086	0.12919	0.00055	−5.1	1266
NOVA88D-17	Harzburgite	Carius Tube	0.76	0.20		0.012	2.04	9.95	2.52	2.53	1.70	0.0344	0.0005	0.12467	0.00021	−1.9	701
NOVA88D-16	Basalt	Carius Tube	15.7	8.63		0.075	1.96	0.378	0.086	0.063	0.015	24.5	0.4	0.17650	0.00105	10.0	
Standard Reference Materials																	
HARZ-01	Harzburgite	Carius Tube				0.066	5.73	7.74	6.08	4.57	3.71	0.08576	0.00257	0.12486	0.00012		
HARZ-01	Harzburgite	Carius Tube				0.053	5.49	6.04	6.65	4.45	3.37	0.07560	0.00227	0.12439	0.00014		
HARZ-01	Harzburgite	Carius Tube				0.055	5.82	9.52	7.62	3.89	4.14	0.06396	0.00192	0.12582	0.00010		
					Average (n = 3)	0.058	5.68	7.77	6.78	4.30	3.74			0.12502			
					St Dev	0.007	0.17	1.74	0.78	0.36	0.39			0.00073			
					RSD	12%	3%	22%	11%	8%	10%			0.6%			
HARZ-01*	Harzburgite				Average (n = 8)	*0.062*	*5.12*	*6.71*	*5.73*	*3.38*	*4.21*			*0.12543*			
					St Dev	*0.023*	*1.60*	*2.69*	*2.19*	*1.36*	*1.30*			*0.00140*			
					RSD	*37%*	*31%*	*40%*	*38%*	*40%*	*31%*			*1.1%*			

*Average and standard deviations for eight separate measurements of HARZ-01 by Carius tube, reported in Day *et al.* (2012). HPA = high-pressure asher

[a]—$\gamma Os_{90Ma} = ([^{187}Os/^{188}Os_{sample(90Ma)}/^{187}Os/^{188}Os_{chondrite(90Ma)}] - 1) \times 100$; Present-day chondritic $^{187}Os/^{188}Os = 0.12757$, $^{187}Re/^{188}Os = 0.3972$ (Shirey & Walker, 1998).

[b]—T_{RD} = Time of relative depletion at time of emplacement as $1/\lambda \times \ln\{([^{187}Os/^{188}Os_{chondrite} - ^{187}Os/^{188}Os_{primitive\ mantle}]/^{187}Re/^{188}Os_{chondrite}) + 1\}$:; Present-day primitive mantle $^{187}Os/^{188}Os = 0.1296$, $^{187}Re/^{188}Os = 0.4243$ (Meisel et al., 2001).

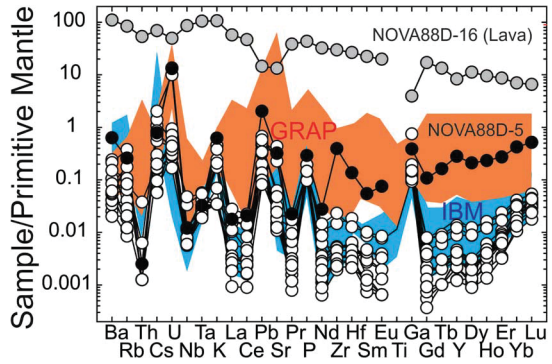

Fig. 8. Primitive mantle normalized incompatible trace element diagram for bulk rock samples from the NOVA88D dredge of the Tonga Trench. Shown for comparison are fields for Gakkel Ridge abyssal peridotites (GRAP; orange) from Day *et al.* (2017b) and Izu-Bonin-Mariana (IBM; blue) forearc peridotites from Parkinson & Pearce (1998). Primitive mantle normalization from McDonough & Sun (1995).

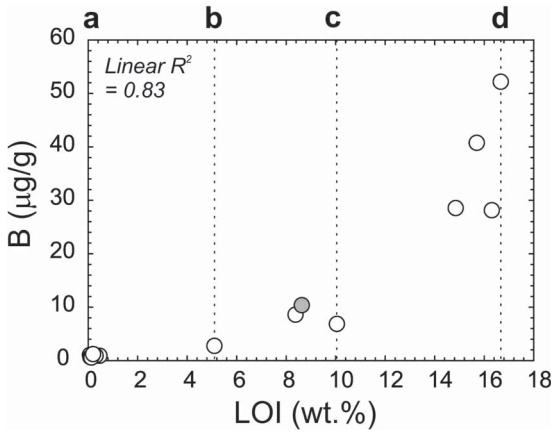

Fig. 9. Diagram illustrating the relationship between LOI values and boron contents in Tonga Trench samples (unfilled circles are peridotites, the grey circle is the lava sample). Shown are the LOI contents for NOVA88D-1 (a), NOVA88D-11 (b), NOVA88D-13 (c), and NOVA88D-15 (d), shown in Fig. 3.

is also much older than the assumed date of subduction initiation at no later than ~52 Ma (Meffre *et al.*, 2012), and is instead closer to the ages of the ~120 Ma Ontong-Java, Manihiki and Hikurangi Plateaus (e.g. Taylor, 2006). Notably, many of the low-Re/Os harzburgite samples show significant scatter and are more likely to reflect isotopic heterogeneity due to more ancient melt depletion events, recorded in the T_{RD} ages (average of 0.7 Ga, excluding D-5), as observed previously in Pacific plate lithosphere (Snortum *et al.*, 2019), and not through ^{187}Re-^{187}Os decay (Fig. 13).

DISCUSSION

Tonga Trench harzburgites from the NOVA88D dredge site have significance for two reasons relevant to this work. First, they experienced varying degrees of serpentinization, allowing appraisal on the effects of these processes on primary peridotite composition, especially related to the HSEs. Second, the Tonga Trench peridotites are highly melt-depleted based on both mineralogy and bulk-rock composition and may record discrete melt depletion or melt refertilization events preceding subduction initiation. Effects of serpentinization and seafloor alteration are first considered, followed by evaluation of the formation of the Tonga Trench peridotites, enabling comparison between these samples and peridotites thought to be formed in mid-ocean ridge and supra-subduction zone settings.

Effects of seafloor alteration and serpentinization

The majority (>90%) of abyssal peridotites collected from the ocean basins have experienced moderate to extensive alteration, either from serpentinization (<400°C) or seafloor weathering (<10°C). Serpentinization results from reaction between seawater and ultramafic rock, following several paths. Serpentinization occurs at low silica activity under reducing conditions (Frost & Beard, 2007), where olivine can be converted to serpentine, magnetite, and brucite (Bach *et al.*, 2004). Serpentinization causes a volume increase (up to 35% in harzburgites, and 48% in dunites) and a decrease in density (from 3.3 g/cm^3 to 2.5 g/cm^3) (Mével, 2003). During these processes there is an associated volatile increase in the serpentinized rock, resulting in water contents ranging from 10 to 15 wt.% (Mével, 2003; Niu, 2004). Serpentinized rocks can be further modified in some tectonic settings from the carbonation of serpentine to talc-magnesite assemblages, leading to loss of Mg or gain of Si, and very high water (>15 wt.%) contents in such 'steatised' rocks (e.g. Day *et al.*, 2017b). Low-temperature seafloor alteration (<10°C) is less pervasive than serpentinization and occurs close to pre-existing fracturing in samples. Low-temperature alteration can occur after serpentinization and is revealed by addition of Mg-rich clays, Fe-oxides, hydroxides, and carbonate minerals in peridotites (Früh-Green *et al.*, 2004). Products of serpentinization are the prevailing alteration products in affected NOVA88D harzburgites.

Seawater composition has a major influence on elements that will be modified during both high and low temperature alteration. Seawater dominantly consists of (>1 mg/L) H, O, Na, Mg, Cl, K, Ca, C, N, S, Sr, Br, F, Si and B. Prior work has shown that serpentinites are enriched in Cl, F, S (Mével, 2003), Si (Malvoisin, 2015) and B (Harvey *et al.*, 2014). Fluid mobility and concentration likely plays a major role in elements that are impacted by serpentinization. Other less abundant and fluid immobile elements are less likely to be strongly impacted.

For this study, LOI is used as a proxy for degree of serpentinization. This parameter, rather than an alteration index (e.g. Birner *et al.*, 2016) was chosen for three reasons. First, there is a strong relationship with visual evidence for serpentinization (Fig.3) and fluid mobile elements, such as B (Fig. 9). Second, LOI is typically measured on almost every published peridotite sample, whereas alteration indices are not always reported, or may be subjective. Similarly, fluid mobile elements or modal abundances of phases are not always reported, or are not reported in a standardized way, such as quantitative (e.g. µg/g) values. Finally, LOI encompasses the loss of volatile compounds at ≥900°C, indicating that H_2O, OH, CO, CO_2 should all be included in this parameter. Using linear regression between LOI and major, minor and trace elements, it is possible to identify those elements most well-correlated with serpentinization in the NOVA88D dredge samples. Sample with R^2 values less than 0.3 are defined as poorly correlated and less than 0.5 as weakly correlated. For the major elements and lithophile to siderophile trace elements, using this definition Si, Ti, Al, Mn, Mg, Sc, V, Cr, Co, Ni, Cu, Zn, Y, Ge, Zr, Nb, Mo, Ba, the REE, Lu, Hf, Ta and Th are all poorly correlated with LOI and—even excluding NOVA88D-5—seem essentially unaffected by alteration processes. Tungsten ($R^2 = 0.45$), Fe_2O_3T ($R^2 = 0.4$), Pb ($R^2 = 0.39$), Cs ($R^2 = 0.38$), Li ($R^2 = 0.37$), P ($R^2 = 0.34$) and Ga ($R^2 = 0.32$) are all weakly correlated.

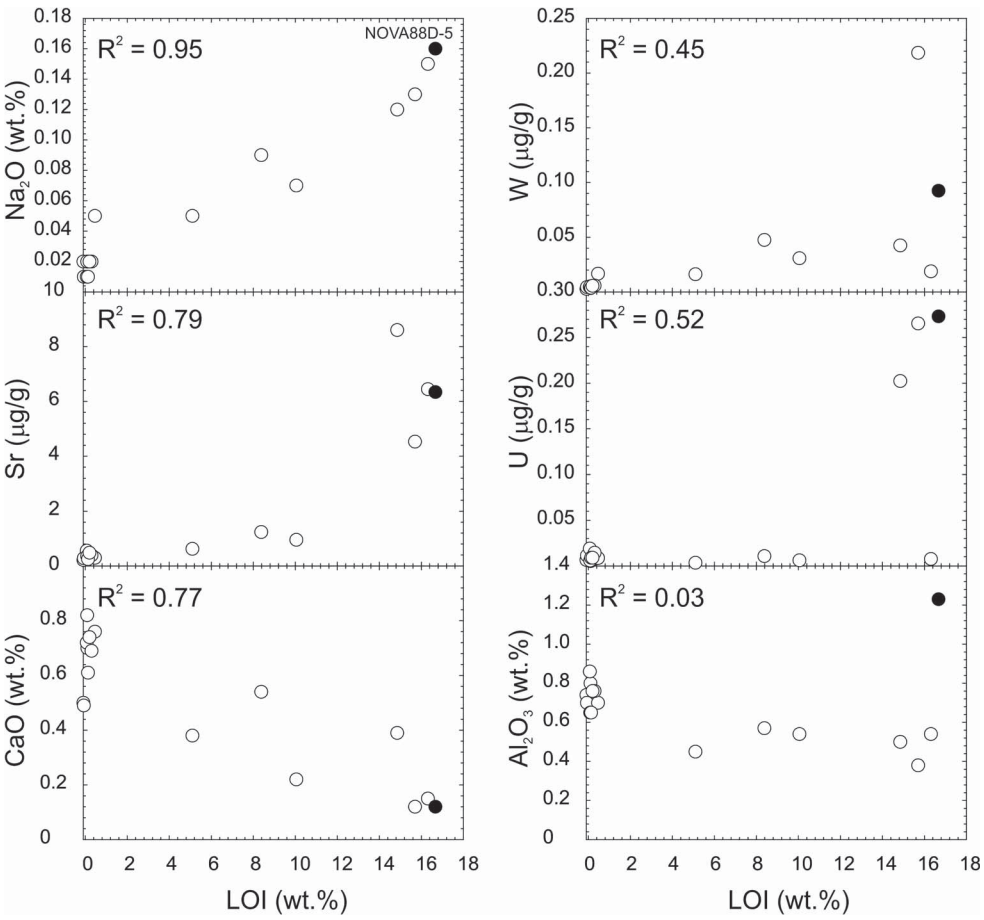

Fig. 10. LOI vs. Na_2O, Sr, CaO, W, U and Al_2O_3 in NOVA88D dredge peridotites. Filled circle denotes anomalous harzburgite NOVA88D-5.

For elements with R^2 values greater than 0.5, we find a general order of correlation between LOI and: Na_2O ($R^2 = 0.95$), B ($R^2 = 0.82$), K_2O ($R^2 = 0.82$), Sr ($R^2 = 0.79$), CaO ($R^2 = 0.77$), Rb ($R^2 = 0.61$) and U ($R^2 = 0.52$). For some elements, such as Na or B, the correlations match a monotonic increase in the concentration of the element with increasing LOI (Figs 9 and 10). However, even for reasonably robust correlations (e.g. U), this relationship is in fact dominated by two or three samples, possibly due to the broadly bimodal nature of the samples as being strongly serpentinized or fresh. All these elements and compounds show a positive correlation with LOI, with the notable exception of CaO, where there is an anticorrelation, possibly through the loss of Ca^{2+} from clinopyroxene during serpentinization (Frost & Beard, 2007).

The data for NOVA88D peridotites are consistent with some elements (e.g. Al, Sc, V, Co, Ni, high field strength elements, the REE) being unaffected by serpentinization, while others are strongly affected (Na, B, K, Sr, Ca, Rb), especially in strongly depleted peridotites. These observations are consistent with prior work noting the importance for fluxes of elements into the mantle during subduction zone processes. Previously, it has been shown that the basaltic portions of down-going lithosphere will have a profound effect on the composition of recycled components in the mantle (e.g. Kelley *et al.*, 2005; Chauvel *et al.*, 2008). For mature oceanic lithosphere, typically the crustal component is ~8% of the total slab, with >90% being peridotite. Although the amount of serpentinization in oceanic lithosphere is typically poorly constrained, this indicates that elements that are enriched in peridotites during serpentinization may be a significant component of elemental fluxes during subduction. These include elements such as the heavy noble gases (e.g. Mukhopadhyay & Parai, 2019). For the NOVA88D peridotites, these elements would include B, W, Sr, and U. Assuming that the abundances of these elements in the NOVA88D peridotites are in some way representative of Tonga Trench lithosphere, then the flux of these elements could represent between 30% and 70% of the total subduction flux. These observations are consistent with enhanced $^{238}U/^{204}Pb$ in recycled oceanic lithosphere being an important contributor to the HIMU signature of some OIB (e.g. Day *et al.*, 2010; Pettke *et al.*, 2018), or to other geochemical features, such as Os isotopes (e.g. Lassiter & Hauri, 1998).

Limited effects of serpentinization on the HSE in oceanic peridotites

A particular concern in studies of seafloor mafic and ultramafic rocks has been the effect of seafloor alteration and serpentinization on the abundances and distributions of the HSE. The HSE are not fluid mobile elements, which means that they should be resilient to hydrothermal alteration in peridotites. Previous studies have examined highly serpentinized samples for Re and Os concentrations and $^{187}Os/^{188}Os$ (Snow & Reisberg, 1995; Harvey *et al.*, 2006; Day *et al.*, 2017b), or compared seafloor altered rinds and fresh cores from Gakkel Ridge peridotites (Liu *et al.*, 2009). Due to the general

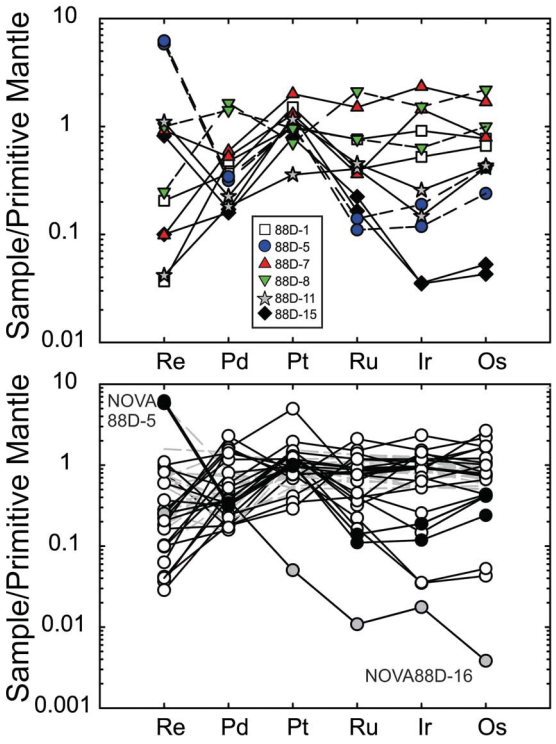

Fig. 11. Primitive mantle normalized HSE diagrams for Tonga Trench peridotites. Upper diagram shows replicate measurements of bulk rock aliquots using Carius tube and HPA digestion methods for the same samples. Lower diagram shows NOVA88D samples vs. abyssal peridotites from the Indian, Atlantic and Arctic ridges. Highlighted are samples NOVA88D-5 (solid fill) and lava sample NOVA88D-16 (grey fill). Abyssal peridotite data and primitive mantle normalization from Day *et al.* (2017b).

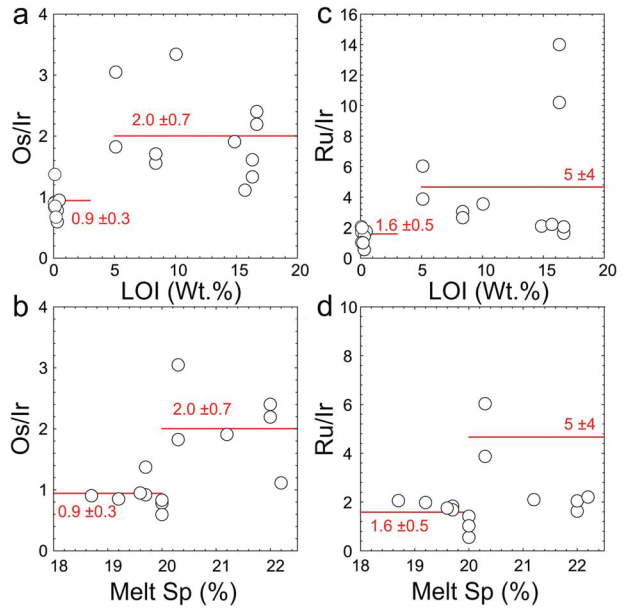

Fig. 12. Comparison of estimates of Os/Ir and Ru/Ir vs. LOI and melt depletion from spinel (Melt Sp) in Tonga Trench peridotites. Higher Os/Ir and Ru/Ir occur in peridotites with both higher LOI and estimates of melt depletion. Fractionation of Os, Ir and Ru at high degrees of melt depletion are consistent with experiments (e.g. Ballhaus *et al.*, 2006) and observations (e.g. Luguet & Reisberg, 2016).

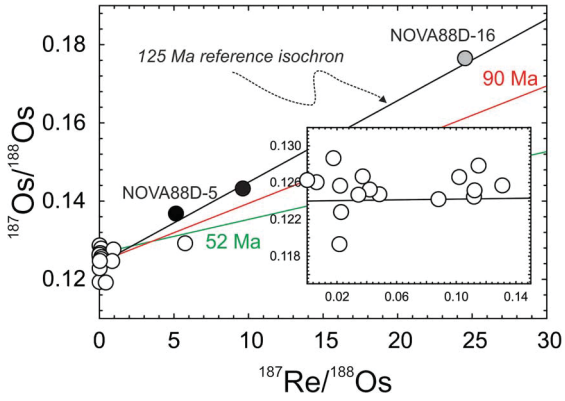

Fig. 13. $^{187}Re/^{188}Os$-$^{187}Os/^{188}Os$ diagram for Tonga Trench samples, showing a 125 Ma reference isochron anchored to an initial mantle $^{187}Os/^{188}Os$ ratio of 0.124. Also shown are 90 Ma and 52 Ma reference isochrons, corresponding to opening of the Osborn Trough and the inferred inception of Tonga Trench subduction, respectively. Symbols are the same as for the lower panel of Fig. 11. Inset shows details of the region on the far left of the host diagram for harzburgite samples. Error bars are smaller than symbols.

lack of availability of fresh oceanic peridotite samples, it has not been possible to examine HSE abundances and Os isotopes variations in a peridotite suite from the same location that exhibit a wide variation in degree of serpentinization.

For the Tonga Trench peridotites there is a general increase in Re and decrease in Pd and Pt abundance variations with increasing LOI, as well as in $^{187}Re/^{188}Os$. Correlations with Re and U, as noted by prior studies examining sea floor alteration (Harvey *et al.*, 2006), are not evident in the Tonga Trench samples. A larger compilation of HSE abundances and LOI in oceanic peridotites reveals no strong correlations (Fig. 14). Instead, there is significant overlap between HSE concentrations measured in relatively unaltered samples with low LOI, and those measured in strongly serpentinized peridotites. All samples show a significant degree of heterogeneity in abundances regardless of degree of serpentinization. For Tonga Trench peridotites, Pt has the largest degree of variance observed in unaltered samples, ranging from 2 to 37 ng/g. Correlation in trends for NOVA88D samples, measured by the R^2 value, is highest for Re ($R^2 = 0.33$). There are no correlations for Pd ($R^2 = 0.19$), Pt ($R^2 = 0.04$), Ru ($R^2 = 0.007$), Ir ($R^2 = 0.09$), and Os ($R^2 = 0.03$). As noted above, fresh Tonga Trench peridotites have lower Os/Ir and Ru/Ir than serpentinized samples, but these peridotites also have generally lower estimated degrees of melt depletion (Fig. 12). The higher Os/Ir in the serpentinized Tonga Trench peridotites is also converse to the trend to lower Os/Ir in Kilbourne Hole samples, attributed to subaerial weathering (Harvey *et al.*, 2015). As with HSE abundances, osmium isotopes are not controlled by serpentinization processes, and have no correlation with LOI ($R^2 = 0.0003$) (Fig. 14). The increased dispersion of $^{187}Os/^{188}Os$ with increasing LOI could be attributed to a greater sampling of serpentinized peridotite populations during dredging operations rather than from alteration effects, a statement supported by the HSE abundances and LOI. Indeed, this statement remains valid even when steatised rocks (LOI >16 wt.%) are included in comparisons (Figs 14 and 15; Day *et al.*, 2017b).

The results of this study, and those of previous works (Snow & Reisberg, 1995; Harvey *et al.*, 2006; Liu *et al.*, 2009; Snortum & Day, 2020) do not provide compelling evidence that seafloor alteration or serpentinization systematically control the HSE abundances or

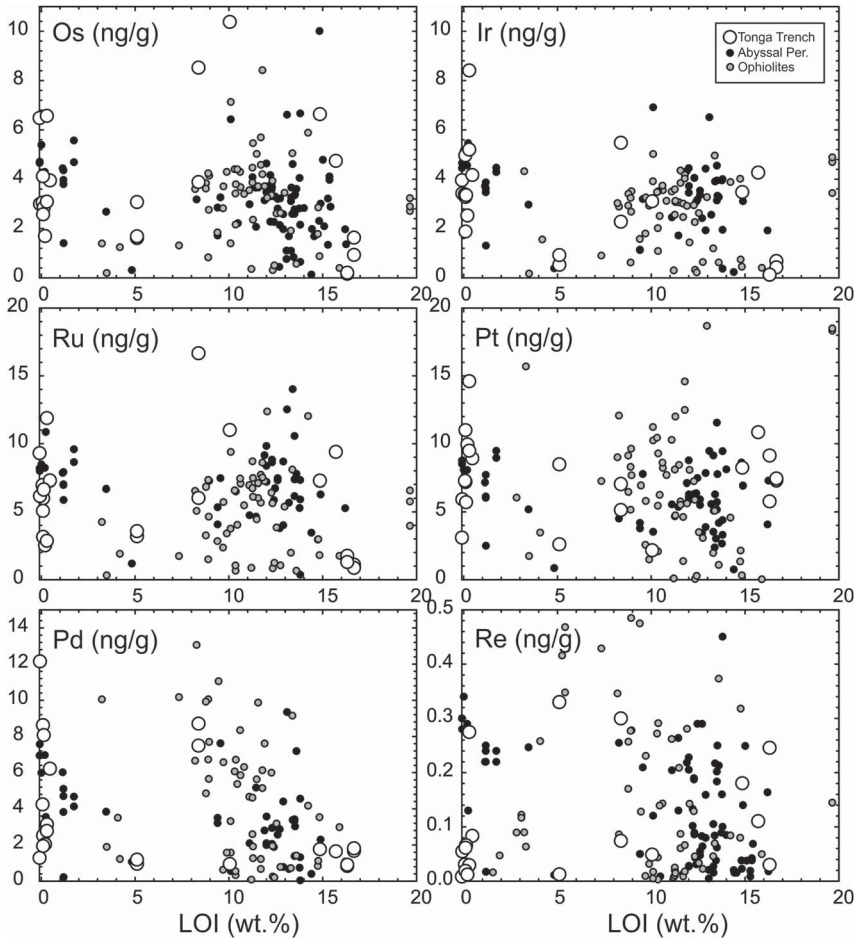

Fig. 14. LOI vs. HSE (Os, Ir, Ru, Pt, Pd, Re) abundances in NOVA88D samples vs. abyssal peridotites (compilation in Day *et al.*, 2017a) and Iapetus-aged ophiolites (Shetland, Leka; O'Driscoll *et al.*, 2012, 2015; Day *et al.*, 2017b). Stippled line shows average 'primitive mantle' composition from Becker *et al.* (2006) and modified by Day *et al.* (2017b).

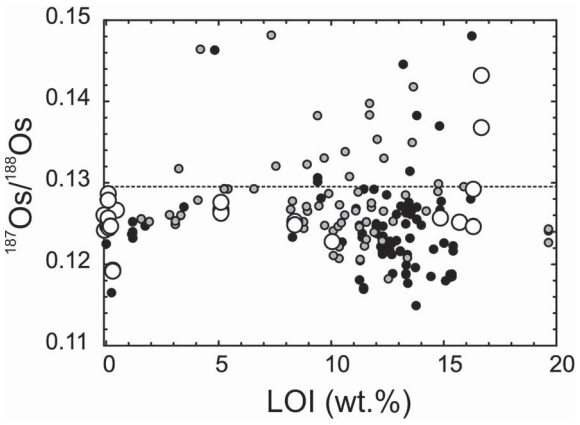

Fig. 15. LOI vs. $^{187}Os/^{188}Os$ in NOVA88D Tonga Trench samples, abyssal peridotites and ophiolites. Stippled line is the estimated primitive mantle $^{187}Os/^{188}Os$ composition. Symbols and data sources are the same as for Fig. 14.

Os isotope composition in oceanic peridotites. Instead, our results expand the results of work by Liu *et al.* (2009) for Gakkel Ridge peridotites. When comparing the weathered rims (LOI ~3 wt.%) to the fresh interiors (~0 wt.% LOI), they found that the concentrations were statistically the same. As noted previously, by Alard *et al.* (2005), concentrations of Os in seawater (~10^{-5} ng/g) are much lower than the average abyssal peridotite (~3 ng/g) requiring significant volumes of seawater (seawater:rock ratios of 1000 to 10 000) to noticeably affect rock concentrations. The NOVA88D peridotites provide strong evidence that the HSE abundance and Os isotopic variations in abyssal peridotites reflect melt-depletion or melt-infiltration signatures during mantle processes, rather than being systematically affected by serpentinization or seawater alteration.

Petrogenesis of Tonga trench peridotites

The NOVA88D Tonga Trench peridotites were dredged in 1967—at the inception of the theory of plate tectonics and well before global positioning systems—making the exact location of the dredge, with >9000 m of extended cable, uncertain. Nonetheless, Fisher & Engel (1969) considered the dredge to come from what is the arc-side of the trench. Later dredges to the north of the NOVA88D dredge site obtained peridotites from the arc-side of the trench, supporting this contention (Bloomer & Fisher, 1987; Bloomer *et al.*, 1996; Wright *et al.*, 2000). Geochemical results presented here also support such a conclusion. The NOVA88D samples are considerably more refractory than typical abyssal peridotites and are more consistent with the

composition of peridotites from northerly dredges in the Tonga Trench (Birner *et al.*, 2017), or from Izu Bonin-Mariana forearc peridotites studied previously (Parkinson & Pearce, 1998; Parkinson *et al.*, 1998).

Important features of Tonga Trench spinel harzburgites from the NOVA88D dredge are that they have low modal clinopyroxene (<3%), U-shaped REE profiles and low absolute incompatible trace element abundances and similar Os concentrations and $^{187}Os/^{188}Os$ values to some forearc peridotites (e.g. Parkinson *et al.*, 1998). Melt refertilization processes are well-documented for oceanic peridotites (e.g. Seyler *et al.*, 2007), but evidence for such effects on the NOVA88D peridotites are limited. The clearest lines of evidence are the U-shaped bulk rock REE patterns in some of the harzburgites. To examine the effects of melt infiltration, modal recombination was performed for the freshest NOVA88D harzburgites (NOVA88D-1, D-3, D-4, D-6, D-9, D-10) by taking the average olivine, orthopyroxene and clinopyroxene trace element abundances measured by LA-ICP-MS. This method assumes all the melt infiltration is cryptic and unassociated with the minerals, and that spinel has only a minor contribution to the modeled incompatible trace elements. The data are plotted logarithmically in Fig. 16 since many of the elements would not be visible on a linear scale. This also means propagated uncertainties from modal analysis (~5% uncertainty) and external uncertainty from LA-ICP-MS (<8%) are not shown. Nonetheless, the similarity between modal recombination using olivine + orthopyroxene ± clinopyroxene and the bulk rock supports only limited melt infiltration effects on samples. Possible exceptions are limited excesses in Ba, La, Ce and Pr. In most cases, the modal recombination suggests trace element abundances in the upper range of bulk rock abundances (Fig. 16). It is important to note that the modal recombinations for rocks with clinopyroxene will incorporate melt infiltration if the clinopyroxene comes from secondary crystallization from melt infiltration. As noted by Birner *et al.* (2017), in their modeling of clinopyroxene compositions, it is difficult to quantify the exact extent of melt refertilization for most samples, but it is limited by the abundance of clinopyroxene. Assuming that the clinopyroxene is secondary, then the degree of melt infiltration will correlate with their modal abundances, from zero to <3%.

Melt infiltration has had no obvious effects on most of the harzburgites in terms of Os isotopes or the HSE. The exception is harzburgite NOVA88D-5 that is distinct from all the other measured samples. This sample has elevated bulk rock REE abundances (Fig. 8) and high $^{187}Re/^{188}Os$ and $^{187}Os/^{188}Os$ (Fig. 12). Notably, the Re-Os isotope systematics of different bulk rock aliquots of NOVA88D-5 plot along an ~125 Ma isochron, along with the basaltic sample analyzed from the same dredge; NOVA88D-16. This basalt is strongly alkalic and does not appear spilitized (assuming Na is inherent to the sample, a basanite composition) with relatively high MgO (9.8 wt.%), TiO_2 (3 wt.%), and has high La/Yb (12) making it distinct both from mid-ocean ridge basalt (MORB), as well as high-MgO rocks from the Tonga Arc (e.g. Falloon *et al.*, 2008; Meffre *et al.*, 2012; Todd *et al.*, 2012). No other samples clearly lie along the isochron line, and the Re-Os isotope compositions for NOVA88D-5 and D-16 cannot be interpreted as being consistent with younger apparent ages.

Samples NOVA88D-5 and D-16 possibly record a Cretaceous magmatic modification event rather than being consistent with the likely age of the subducting plate (~90 Ma; Downey *et al.*, 2007), or inception of subduction in the Tonga Trench at ~52 Ma (e.g. Meffre *et al.*, 2012). The most significant known magmatic event occurring in the region during the Cretaceous was the formation of

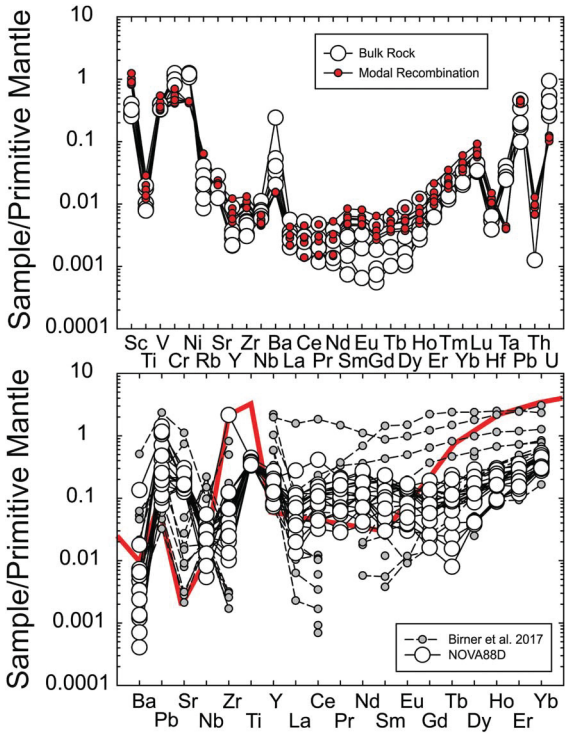

Fig. 16. Primitive mantle normalized plots of unserpentinized bulk rocks and their modal recombination from NOVA88D (upper), and comparison of clinopyroxene abundance data from fresh NOVA88D harzburgites vs. Tonga Trench clinopyroxene data from Birner *et al.* (2017). The modal recombinations were done by taking the model abundances of olivine, orthopyroxene and clinopyroxene (Table 1) and the average abundances of these mineral phases measured in the data set, after removing olivine grains with high apparent Sc. The lower plot shows in red the model results for melting and melt addition from Birner *et al.* (2017) assuming 18% melt depletion and < 0.005% melt addition. These authors showed that the input melt composition is minor such that melt-rock reaction is minimal in samples. Primitive mantle normalization from McDonough & Sun (1995). Error bars are not shown but are ±8%.

the Ontong Java-Manihiki-Hikurangi large igneous province (Taylor, 2006). This event produced vast quantities of basaltic melt products that led to the formation of an oceanic plateau, with subsequent break-up during plate tectonic configuration at ~90 Ma (Downey *et al.*, 2007). Basaltic melts in these events are tholeiitic in compositions ranging from ~7 to 11 wt.% MgO and ~1 wt.% TiO_2 (e.g. Fitton and Godard 2004; Golowin *et al.*, 2018), so are distinct from the composition of NOVA88D-16. Nonetheless, the Re-Os isotope evidence implies that formation of this sample, and melt refertilization in NOVA88D-5, took place at around this time. Particularly notable in this observation is that any subsequent melting or processing after ~120 Ma did not erase evidence for these events.

In contrast with melt refertilization, melt depletion is overwhelmingly evident in the peridotites, from their harzburgite mineralogy, refractory bulk compositions, with low Al_2O_3, and the high Cr# recorded in spinel (Fig. 5). In fact, the Cr-rich nature of the spinel in the Tonga Trench samples, and the more incompatible element-depleted nature of the samples, compared with Izu-Bonin-Mariana forearc peridotites make them an extreme endmember for dredge oceanic peridotites. Calculation of melt depletion using spinel compositions and employing the empirical calculation method of

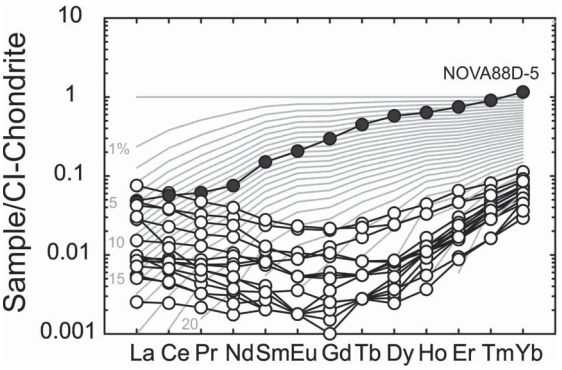

Fig. 17. CI-chondrite normalized plot of NOVA88D dredge harzburgites analyzed in this study. Gray lines indicate 1% melt increments for a non-modal fractional melting model, where increasing melt depletion results in lower absolute abundances of the REE and increasing depletion in the LREE relative to HREE. Model parameters and normalization are provided in Day *et al.* (2017b).

Hellebrand *et al.* (2001) are consistent with the NOVA88D peridotites having experienced between ~18% and 22% partial melt loss, assuming a fertile mantle starting composition. These estimates of partial melt loss are much greater than for abyssal peridotite spinel which typically record evidence for ~10% partial melt loss (Warren, 2016), and range between 2% and 16% (D'Errico *et al.*, 2016; Day *et al.*, 2017a; Paquet *et al.*, 2021). Similar estimates for melt loss can be obtained from modeling of middle and heavy REE abundances in bulk rocks unaffected by melt refertilization (i.e. NOVA88D-5), revealing >20% partial melt loss for the Tonga Trench peridotites (Fig. 17). These melt loss estimates are higher than clinopyroxene based estimates which indicate between ~14% and 18% melt loss (Birner *et al.*, 2017). Modeling of near-fractional melting suggests that a spinel Cr# of 60 is an upper boundary corresponding to ~18 to 20% melt extraction, where clinopyroxene is exhausted during peridotite partial melting (e.g. Hirschmann *et al.*, 1998). For these reasons, the rare clinopyroxene grains found within samples are unlikely to record the significant melt loss observed from spinel compositions or bulk rock REE abundances, with the implication that the clinopyroxene grains may be secondary from limited melt infiltration by depleted melts. Such a mode of origin for the clinopyroxene would be consistent with the modal recombination of rocks, since the clinopyroxene is an inherent part of the mineralogy in some studied peridotites.

The high degrees of melt loss experienced by the NOVA88D harzburgites are consistent with the observed HSE abundances in the samples. The HSE are mainly hosted by sulphides in fertile mantle samples, with exhaustion of sulphide during melt depletion of peridotites leading to the release of more incompatible HSE (e.g. Re, Pt, Pd) into the melt, and the sequestration of more compatible HSE (e.g. Ru, Ir, Os) into HSE-rich residual sulphide and alloy phases (e.g. Luguet & Reisberg, 2016). Assuming a fertile mantle composition has 250 μg/g S (e.g. McDonough & Sun, 1995) then complete S exhaustion in harzburgite residues occurs as ~23% partial melt loss (Day, 2013), which is at approximately the same degree of melt depletion observed for some NOVA88D harzburgites. Melt depletion is known to result in harzburgites having more heterogenous distribution of the HSE than lherzolites (e.g. Luguet & Reisberg, 2016), due to the presence of micro-inclusions of HSE-rich sulphides and alloys formed during partial melting and melt-rock reaction. The absence of observable sulphides in polished thin sections of fresh NOVA88D harzburgites and the heterogenous HSE abundances of replicate analyses of bulk rock sample powders (Fig. 11a) are consistent with nugget heterogeneities from alloys within the samples. Several harzburgites (D-5, D-11, D-15) show relative depletions in Os, Ir and Ru relative to primitive mantle (Fig. 11). Furthermore, the most extensive melt depleted peridotites also have the highest Os/Ir and Ru/Ir, consistent with preferential retention of Os and Ru relative to Ir in the samples (Fig. 12). These fractionations are consistent with progressive exhaustion of sulphur in the source during melting and stabilization of Os, Ir, Ru-rich phases (Ballhaus *et al.*, 2006), but are opposite to observations of loss of Os and Ru from Ir, likely during alloy stabilization in peridotites (e.g. Kepezhinskas & Defant, 2001; Lorand & Luguet, 2016; O'Driscoll & González-Jiménez, 2016; Snortum & Day, 2020). The cause of these differences requires further investigation. One possibility is that more reducing conditions of melting occurred within the Tonga Trench peridotites resulting in distinct behavior of the redox sensitive elements, Os and Ru. This would be consistent with the low Os/Ir and Ru/Ir measured in Point Sal ophiolite peridotites, interpreted to have experienced melt depletion in an oxidizing forearc environment (Snortum & Day, 2020),

Did Tonga Trench peridotites form in the modern forearc?

The straight-forward interpretation of the NOVA88D peridotites is that, as with Tonga Trench peridotites in general (Birner *et al.*, 2017), they have been minimally affected by melt refertilization and are the products of significant melt depletion (>18%). These depletions have been interpreted to reflect that Tonga Trench harzburgites, which are exposed on the trench wall of the overriding plate, are forearc peridotites, recording processes occurring during and following subduction initiation to form the Tonga arc (Birner *et al.*, 2017). A notable aspect of the new Re-Os isotope data for the NOVA88D peridotites, however, is that all the harzburgites record evidence for melt depletion events well before 52 million years ago, with some recording a possible Cretaceous melt refertilization event (NOVA88D-5; section 4.3), with the average T_{RD} age of the suite at 710 ± 350 million years, with some harzburgites with T_{RD} ages as ancient as 1500 million years.

A critical question is when the bulk of melt depletion took place in the harzburgites. For example, the ancient T_{RD} ages in the harzburgites might merely be recorded because extensive melt depletion in the forearc led to removal of the majority of the HSE, as recorded in the spinel compositions and bulk rock REE abundances. This would lead to only residual Os-rich and Re-poor alloys that stabilized in the rock during a prior episode of melt depletion. In this case, processes recorded in the peridotites would likely reflect conditions in the Tonga forearc. Alternatively, it is possible that the most extensive melt depletion in the harzburgites occurred prior to their incorporation into the overriding plate. In this scenario, the peridotites act as refractory residues, uninvolved in modern forearc processes and the extensive melt depletion in the samples is not related to the conditions of their recent tectonic environment.

There are several lines of evidence that favor the latter—not the former—explanation. In the first instance, the apparent Cretaceous refertilization event in NOVA88D-5 would suggest that any later melt depletion events in the forearc may not have been efficient at eradicating this prior history. Secondly, samples with old T_{RD} ages

(>500 Ma) record >18% melt depletion (from spinel compositions), and can have some of the highest Ru, Ir and Os contents and highest Os/Ir and Ru/Ir of the sample set. This would be most consistent with ancient melt depletion in harzburgites leading to heterogenous HSE distributions, rather than modern melt depletion beneath the Tonga arc. Finally, the range in $^{187}Os/^{188}Os$ measured in the harzburgites is similar to that observed both for global abyssal peridotites (Day *et al.*, 2017a; Paquet *et al.*, 2021), within Izu-Bonin-Mariana forearc xenoliths (Parkinson *et al.*, 1998), as well as for Pacific mantle rocks in general (Snortum *et al.*, 2019; Paquet *et al.*, 2021). These heterogeneous Os isotope distributions within Pacific mantle are remarkably distinct from the mantle sections of the Point Sal or New Caledonia ophiolites that have been shown to have formed in a forearc setting (Liu *et al.*, 2018; Secchiari *et al.*, 2020; Snortum & Day, 2020). Peridotites from these ophiolites do not have particularly ancient melt depletion ages, despite having experienced >20% melt depletion, suggesting their derivation from relatively fertile asthenospheric protoliths (Snortum & Day, 2020). The Tonga Trench peridotites appear quite distinct from this mode-of-origin, and indications are that they were significantly melt depleted prior to being incorporated into their present tectonic configuration.

Implications for redox conditions beneath the modern Tonga Trench

Oxygen fugacity (fO_2) is an intensive variable that controls the geochemical behavior of redox-sensitive elements such as Fe, V, Cr, S, C and H. It has been well-established that fO_2 in arc basalts are elevated by $\sim+1$ to $+5$ log units ΔFMQ above ambient mantle, with likely cause(s) being from subduction-related metasomatism of their mantle source, or from differentiation and degassing processes (Lee *et al.* 2005; Kelley & Cottrell, 2009; Brounce *et al.*, 2014). Studies of peridotites from subduction zones and some forearcs suggest that the subducting mantle is likely to be oxidized (Brandon & Draper, 1996; Parkinson & Pearce, 1998; Parkinson *et al.*, 2003) relative to the MORB mantle source (e.g. Bryndzia & Wood, 1990). Birner *et al.* (2017) concluded that the Tonga Trench peridotites represented forearc peridotites and were less pervasively influenced by oxidation related to subduction processes than previously reported.

The NOVA88D harzburgites reported in this study have similar fO_2 and equilibration temperatures to those reported by Birner *et al.* (2017) (Fig. 18). Calculations were performed in an identical fashion to those completed in that study, assuming phase equilibrium between olivine, orthopyroxene, and spinel, using the fO_2 method described in Davis *et al.* (2017), and using the two pyroxene and calcium-in-orthopyroxene thermometers of Brey & Köhler (1990), and the olivine-spinel thermometer of Li *et al.* (1995). For consistency with prior work (e.g. Birner *et al.*, 2017), pressures of equilibration were assumed to be 0.6 GPa. Particularly notable in these comparisons are that Tonga Trench peridotites have similar fO_2 to abyssal peridotites at $\sim-0.4\pm0.4$ ΔFMQ and generally lower than in subduction related peridotite compositions (Fig. 18). The estimated temperatures of equilibration from olivine and spinel are relatively low at $\sim830\pm120$ °C and similar to those reported for Tonga Trench peridotites (874 ± 73 °C; Birner *et al.*, 2017), and are similar to abyssal peridotites (between 840 and 950 ± 50 °C; Bryndzia & Wood, 1990; data from Paquet *et al.*, 2021). As discussed in the previous section, however, the ancient T_{RD} ages of some of these rocks suggest that the estimated fO_2 compositions may not in fact be representative

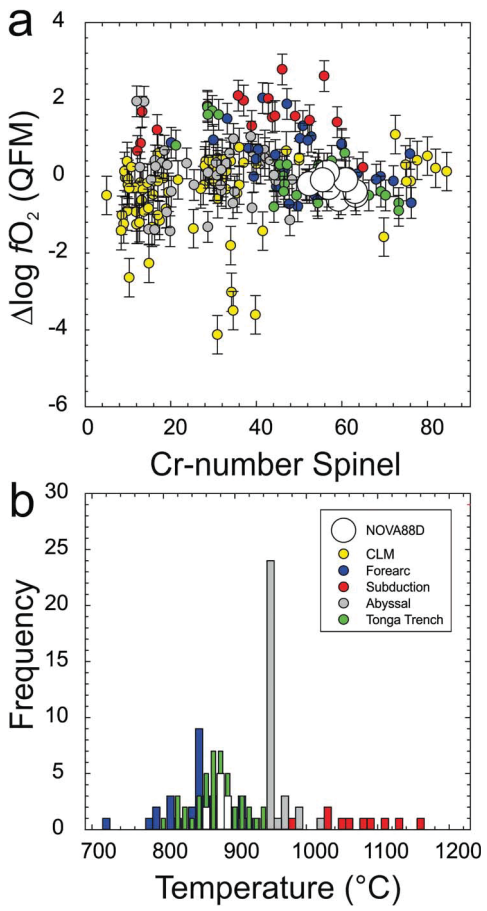

Fig. 18. (a) Plot of oxybarometry vs. Cr-number of spinels for Tonga Trench peridotites vs. abyssal peridotite, subduction peridotite xenoliths, forearc peridotite and continental peridotite data from Bryndzia & Wood (1990), Parkinson & Pearce (1998), Parkinson *et al.* (2003), recalculated by Birner *et al.* (2017) and Wang *et al.* (2008, 2013) and Woodland *et al.* (2021). Estimate of continental lithospheric mantle from Parkinson & Pearce (1998). (b) Histogram diagram of equilibration temperatures in the same samples. Thermo-oxybarometry is from olivine-spinel-orthopyroxene equilibration.

of modern forearc mantle. Instead, the estimated temperatures of equilibration and fO_2 may reflect both ancient melt depletion and more recent modification, such as melt infiltration processes, that have occurred in the samples.

An alternative means with which to compare fO_2 and melting conditions in peridotites was proposed by Parkinson & Pearce (1998) who developed melt depletion models based on Ti-V-Yb abundance systematics (Fig. 19). Using the same methods, Tonga Trench peridotites can be compared along with Izu-Bonin-Mariana forearc rocks and forearc ophiolite mantle from Point Sal. The fO_2 and partial melting constraints from these models are consistent with estimates from mineral compositions, at <0 ΔFMQ and extensive melt depletion in the spinel stability field for Tonga Trench peridotites, with similar conditions for Izu-Bonin-Mariana forearc peridotites with ancient T_{RD} ages. However, both these locations lack radiogenic $^{187}Os/^{188}Os$ like some Point Sal peridotites and other sub-arc mantle wedge peridotites (Brandon *et al.*, 1996; Saha *et al.*, 2005; Widom *et al.*, 2003; Snortum & Day, 2020). Experimental data (Xiong & Wood, 2000; Righter *et al.*, 2002) and observations have been used

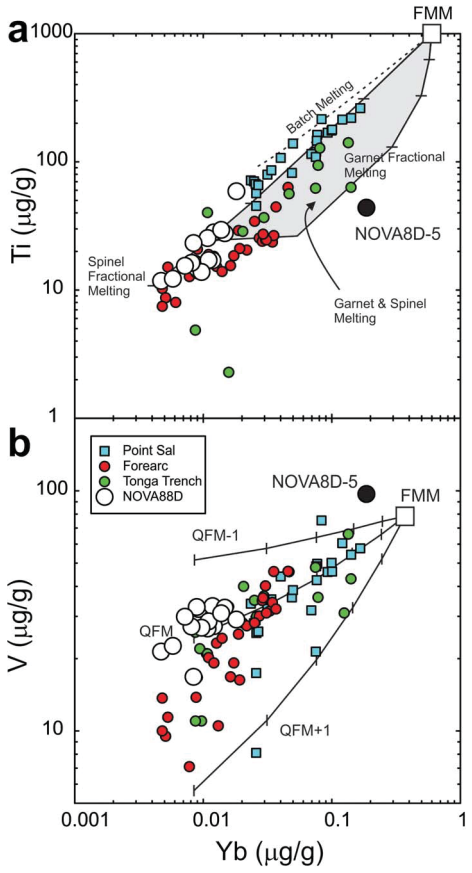

Fig. 19. Plots of (a) Ti vs. Yb and (b) V vs. Yb for NOVA88D and Tonga Trench peridotites (this study; Birner *et al.*, 2017) vs. forearc peridotites (Parkinson & Pearce, 1998) and the forearc Point Sal ophiolite (Snortum & Day, 2020). Modeled melt extraction and oxygen fugacities (quartz-magnetite-fayalite [QFM] buffer) are from Parkinson & Pearce (1998). Theoretical composition of fertile MORB mantle is shown as FMM. In the spinel stability field, both Ti and Yb are highly incompatible. In the garnet stability field, extraction of Yb into the melt is suppressed relative to Ti, because of its favorable incorporation into garnet such that it behaves instead as a slightly incompatible, or even compatible element (Pearce & Parkinson, 1998). In mid-ocean ridge settings (~QFM to QFM-1; quartz-fayalite-magnetite buffer), V behaves as a moderately incompatible element, whereas under the more oxidizing conditions that may occur during SSZ melting of peridotites modified by aqueous fluids rising from the down-going slab (~QFM + 1), V acts as a highly incompatible trace element.

to propose that the radiogenic ^{187}Os originates from slab derived Cl-rich, oxidized fluids, where there is increasing solubility of Os. These are quite distinct from the peridotites interpreted to have come from forearc settings such as the Tonga Trench (Birner *et al.*, 2017), or the Izu-Bonin-Mariana region (Parkinson & Pearce, 1998; Parkinson *et al.*, 1998). Consequently, the fO_2 conditions in the NOVA88D samples may not be recording conditions in the forearc, but rather prior melting conditions, or an amalgamation of processes.

Ancient refractory residues caught up in continuing upper mantle processes

The ancient rhenium depletion ages for both Tonga Trench and Izu-Bonin-Mariana mantle rocks might suggest that geochemical features within them (e.g. calculated fO_2 and melt depletion estimates) may not record conditions acting in recent forearc mantle with fidelity. Instead, these peridotites can be interpreted to represent previously strongly melt-depleted residue accidentally caught up in its present tectonic setting. As such, the high extents of melt depletion will not relate to fluid-assisted melting in these particular cases. Instead, the peridotites may represent refractory residues that played a limited role in melt production beneath their respective arcs. While such a conclusion might contradict prior work on peridotites like those found in the Tonga Trench and Izu-Bonin-Mariana forearc, it is also consistent with ongoing studies of general mantle melt depletion and may inform on models for the formation of continental lithosphere.

Ancient melt depletion in the oceanic mantle is now well described for abyssal peridotites (Harvey *et al.*, 2006; Müntener & Manatschal, 2006; Lassiter *et al.*, 2014; Day *et al.*, 2017a; McCarthy *et al.*, 2018; Sanfilippo *et al.*, 2019; Paquet *et al.*, 2021) and in oceanic mantle xenoliths (Bizimis *et al.*, 2007; Simon *et al.*, 2008; Jackson *et al.*, 2016; Snortum *et al.*, 2019). The ancient T_{RD} ages, extending to as ancient as ~2 Ga, have been interpreted to reflect heterogeneities in the HSE imparted by earlier melt depletion events either at mid ocean ridges, during subduction, or even from plume influence, that have been stirred into the convecting mantle through Wilson cycles. Evidence from ophiolites suggests that, of all these potential melting regimes, subduction zones and particularly forearcs are likely to lead to the greatest extents of partial melting (e.g. O'Driscoll *et al.*, 2012, 2015; Liu *et al.*, 2018; Snortum & Day, 2020). In this respect, the NOVA88D harzburgites have variable to high Os contents, low Al_2O_3 and unradiogenic $^{187}Os/^{188}Os$, similar to supra-subduction zone peridotites (Fig. 20). In the case of the Tonga Trench peridotites, they have exhibited some of the greatest extents of melt loss of all known oceanic peridotites, but the evidence from Re-Os isotopes favors these events occurring long before they became entrained into the Tonga arc. Consequently, the origin of these rocks as deriving from subduction melting processes is possible, but this most likely did not occur in the arc setting they are currently within. In turn, these rocks would not be source rocks to volcanic products found within the Tonga arc region. This conclusion is consistent with those from other locations where the underlying mantle and overlying crustal rocks are not genetically related (e.g. Rampone *et al.*, 1998; McCarthy *et al.*, 2018).

Another feature of the Tonga Trench peridotites is that their refractory spinel compositions and fO_2 lie within the range of the more refractory continental lithospheric mantle compositions reported previously (e.g. Ballhaus, 1993; Parkinson & Pearce, 1998; Wang *et al.*, 2008, 2013; Woodland *et al.*, 2021). Continental lithospheric mantle is considered to have fO_2 between 0 ΔFMQ and −4 ΔFMQ, with shallower-derived spinel peridotites generally recording higher fO_2 than garnet peridotites (Stagno & Fei, 2020). Models for continental lithospheric mantle formation have invoked substantial melt extraction of mantle residues either by deep plume melting (Boyd, 1989; Griffin *et al.*, 1998), shallow melting and subduction (e.g. Schulze, 1986; Canil & Wei, 1992), or through lithospheric melt extraction prior to subduction stacking (Canil, 2004; Simon *et al.*, 2008). Peridotites such as those from the Tonga Trench indicate that strongly depleted melt residues have been readily formed by shallow fluid-assisted melting within subduction zones from the Proterozoic to the present-day and may be quite extensive based on studies of ophiolites as well as oceanic peridotites in general. These results would be consistent with shallow melting and subduction or subduction stacking of depleted lithosphere to form continental lithosphere, while strongly depleted residues can also occur with subduction zones and at mid-ocean ridges.

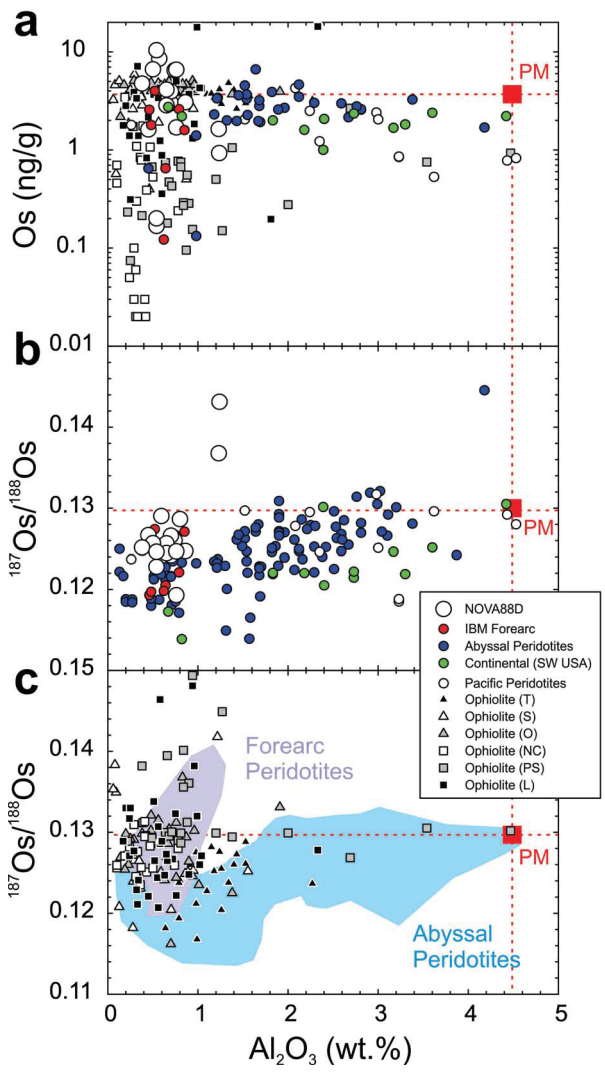

Fig. 20. Diagrams of Al_2O_3 vs. (a) Os concentration and (b, c) $^{187}Os/^{188}Os$ for Tonga Trench peridotites vs. peridotites from a range of tectonic settings, including abyssal peridotites (Day *et al.*, 2017b), Pacific forearc peridotites (Parkinson *et al.*, 1998), Pacific plate peridotites (Snortum *et al.*, 2019), ophiolite peridotites (Schulte *et al.*, 2009; Hanghøj *et al.*, 2010; O'Driscoll *et al.*, 2012, 2015; Snortum & Day, 2020) and continental (SW USA) peridotites (Byerly & Lassiter, 2012). Panel b shows Tonga Trench sample vs. abyssal peridotites, Pacific oceanic peridotites and forearc peridotites. Panel c shows the relationship of ophiolites including Taitao, Chile (T), Shetland, Scotland (S), Oman (O), New Caledonia (NC), Point Sal, California (PS) and Leka, Norway (L).

CONCLUSIONS

Harzburgites from the Tonga Trench that experienced varying degrees of serpentinization enable the examination of both the petrogenetic processes acting upon them and effects of serpentinization. This study has revealed that:

1. Serpentinization has had limited effect on Si, Ti, Al, Mn, Mg, Sc, V, Cr, Co, Ni, Cu, Zn, Y, Ge, Zr, Nb, Mo, Ba, the REE, Lu, Hf, Ta and Th in the studied samples, but is correlated with Na, B, K, Sr, Ca, Rb, U, and weakly correlated with W, Fe, Pb, Cs, Li P and Ga abundances.
2. Serpentinization has had no systematic effect on the HSE abundances and $^{187}Os/^{188}Os$ compositions in the harzburgites.
3. The NOVA88D harzburgites record evidence that they are strongly melt depleted (>18%), which has resulted in the heterogenous distribution of the HSE within samples. Time of rhenium depletion ages recorded by Os isotopes average ~0.7 ± 0.4 Ga and can be as ancient as 1.5 Ga.
4. A few of the harzburgites, and the lava sample from the associated dredge, suggest melt infiltration processes have modified some incompatible trace element compositions, with at least one melt infiltration event probably at ~120 Ma, prior to the inception of subduction at the Tonga Trench at ~52 Ma.
5. Evidence for ancient melt depletion, combined with evidence for limited melt processing since inception of subduction suggests that the NOVA88D peridotites represent melt residues incorporated into the Tonga arc, rather than their geochemical signatures being produced during processes beneath the modern arc itself.
6. The similar estimates of fO_2 (~ −0.4 ± 0.4 ΔFMQ), as well as similarities in melt depletion ages obtained using Os isotopes with abyssal peridotites and Izu-Bonin-Mariana peridotites suggests that refractory residues from prior melt depletion events are common in the convecting mantle and are likely formed during extensive fluid-assisted melting beneath arcs. These refractory peridotites can be incorporated into a range of tectonic settings, including into later arcs or within the continental lithospheric mantle.

ACKNOWLEDGEMENTS

This work was largely supported by a University of California San Diego Academic Senate Award, and in part, by the NSF Petrology and Geochemistry program (NSF EAR 1447130 and EAR 1918322). Professors Robert Fisher, Jeff Gee and Pat Castillo are thanked for discussions about the NOVA samples. We especially appreciate Robert Fisher for pointing out the remarkable freshness of the NOVA88D peridotite sample sitting on his desk and that captured our interest. Review and editorial comments from Jason Harvey, B. Ronald Frost and Othmar Müntener are greatly appreciated.

REFERENCES

Alard, O., Luguet, A., Pearson, N. J., Griffin, W. L., Lorand, J.-P., Gannoun, A., Burton, K. W. & O'Reilly, S. Y. (2005). In situ Os isotopes in abyssal peridotites bridge the isotopic gap between MORBs and their source mantle. *Nature*, **436**, 1005–1008.

Bach, W., Garrido, C. J., Paulick, H., Harvey, J. & Rosner, M. (2004). Seawater-peridotite interactions: First insights from ODP leg 209, MAR 15°N. *Geochemistry, Geophysics, Geosystems*, **5**. https://doi.org/10.1029/2004GC000744.

Ballhaus, C. (1993). Redox states of lithospheric and asthenospheric upper mantle. *Contributions to Mineralogy and Petrology*, **114**, 331–348.

Ballhaus, C., Bockrath, C., Wohlgemuth-Ueberwasser, C., Laurenz, V. & Berndt, J. (2006). Fractionation of the noble metals by physical processes. *Contributions to Mineralogy and Petrology*, **152**, 667–684.

Becker, H., Horan, M. F., Walker, R. J., Gao, S., Lorand, J.-P. & Rudnick, R. L. (2006). Highly siderophile element composition of the Earth's primitive upper mantle: constraints from new data on peridotite massifs and xenoliths. *Geochimica et Cosmochimica Acta*, **70**, 4528–4550.

Bénard, A., Müntener, O., Pilet, S., Arculus, R. J. & Nebel, O. (2021). Silica-rich spinel harzburgite residues formed by fractional hybridization-melting of the intra-oceanic supra-subduction zone mantle: new evidence from TUBAF seamount peridotites. *Geochimica et Cosmochimica Acta*, **293**, 477–506.

Bevis, M., Taylor, F. W., Schutz, B. E., Recy, J., Isacks, B. L., Helu, S., Singh, R., Kendrick, E., Stowell, J., Taylor, B. & Calmantli, S. (1995). Geodetic observations of very rapid convergence and back-arc extension at the Tonga arc. *Nature*, **374**, 249–251.

Bloomer, S. H. & Fisher, R. L. (1987). Petrology and geochemistry of igneous rocks from the Tonga trench: a non-accreting plate boundary. *The Journal of Geology*, **95**, 469–495.

Bloomer S. H., Wright, D. J., MacLeod, C. J. *et al.* (1996). Geology of the Tonga forearc: a supra-subduction zone ophiolite. *EOS Transactions American Geophysical Union OG32B-01*.

Birner, S. K., Warren, J. M., Cottrell, E. & Davis, F. A. (2016). Hydrothermal alteration of seafloor peridotites does not influence oxygen fugacity recorded by spinel oxybarometry. *Geology*, **44**, 535–538.

Birner, S. K., Warren, J. M., Cottrell, E., Davis, F. A., Kelley, K. A. & Falloon, T. J. (2017). Forearc peridotites from Tonga record heterogeneous oxidation of the mantle following subduction initiation. *Journal of Petrology*, **58**, 1755–1780.

Bizimis, M., Griselin, M., Lassiter, J. C., Salters, V. J. & Sen, G. (2007). Ancient recycled mantle lithosphere in the Hawaiian plume: osmium–hafnium isotopic evidence from peridotite mantle xenoliths. *Earth and Planetary Science Letters*, **257**, 259–273.

Boyd, F. R. (1989). Compositional distinction between oceanic and cratonic lithosphere. *Earth and Planetary Science Letters*, **96**, 15–26.

Boyd, F. R. & Mertzman, S. A. (1987) Composition and structure of the Kaapvaal lithosphere, southern Africa. In: (Mysen B. O. (ed)) *Magmatic Processes: Physicochemical Principles: Geochemical Society Special Publications*, London, Vol. **1**, pp. 13–24.

Brandon, A. D. & Draper, D. S. (1996). Constraints on the origin of the oxidation state of mantle overlying subduction zones: an example from Simcoe, Washington, USA. *Geochimica et Cosmochimica Acta*, **60**, 1739–1749.

Brandon, A. D., Creaser, R. A., Shirey, S. B. & Carlson, R. W. (1996). Osmium recycling in subduction zones. *Science*, **272**, 861–863.

Brandon, A. D., Snow, J. E., Walker, R. J., Morgan, J. W. & Mock, T. D. (2000). ^{190}Pt-^{186}Os and ^{187}Re-^{187}Os systematics of abyssal peridotites. *Earth and Planetary Science Letters*, **177**, 319–335.

Brey, G. P. & Köhler, T. (1990). Geothermobarometry in four-phase lherzolites II. New thermobarometers, and practical assessment of existing thermobarometers. *Journal of Petrology*, **31**, 1353–1378.

Brounce, M. N., Kelley, K. A. & Cottrell, E. (2014). Variations in $Fe^{3+}/\sum Fe$ of Mariana arc basalts and mantle wedge fO_2. *Journal of Petrology*, **55**, 2513–2536.

Bryndzia, L. T. & Wood, B. J. (1990). Oxygen thermobarometry of abyssal spinel peridotites: the redox state and C–O–H volatile composition of the Earth's sub-oceanic upper mantle. *American Journal of Science*, **290**, 1093–1116.

Byerly, B. L. & Lassiter, J. C. (2012). Evidence from mantle xenoliths for lithosphere removal beneath the Central Rio Grande Rift. *Earth and Planetary Science Letters*, **355**, 82–93.

Canil, D. (2004). Mildly incompatible elements in peridotites and the origins of mantle lithosphere. *Lithos*, **77**, 375–393.

Canil, D. & Wei, K. (1992). Constraints on the origin of mantle-derived low Ca garnets. *Contributions to Mineralogy and Petrology*, **109**, 421–430.

Chauvel, C., Lewin, E., Carpentier, M., Arndt, N. T. & Marini, J. C. (2008). Role of recycled oceanic basalt and sediment in generating the Hf–Nd mantle array. *Nature Geoscience*, **1**, 64–67.

Cooperdock, E. H., Raia, N. H., Barnes, J. D., Stockli, D. F. & Schwarzenbach, E. M. (2018). Tectonic origin of serpentinites on Syros, Greece: geochemical signatures of abyssal origin preserved in a HP/LT subduction complex. *Lithos*, **296**, 352–364.

Davis, F. A., Cottrell, E., Birner, S. K., Warren, J. M. & Lopez, O. G. (2017). Revisiting the electron microprobe method of spinel–olivine–orthopyroxene oxybarometry applied to spinel peridotites. *American Mineralogist*, **102**, 421–435.

Day, J. M. D. (2013). Hotspot volcanism and highly siderophile elements. *Chemical Geology*, **341**, 50–74.

Day, J. M. D., Floss, C., Taylor, L. A., Anand, M. & Patchen, A. D. (2006). Evolved mare basalt magmatism, high mg/Fe feldspathic crust, chondritic impactors and the petrogenesis of Antarctic lunar meteorites Meteorite Hills 01210 and Pecora escarpment 02007. *Geochimica et Cosmochimica Acta*, **70**, 5957–5989.

Day, J. M. D., Pearson, D. G., Macpherson, C. G., Lowry, D. & Carracedo, J. C. (2010). Evidence for distinct proportions of subducted oceanic crust and lithosphere in HIMU-type mantle beneath El Hierro and La Palma, Canary Islands. *Geochimica et Cosmochimica Acta*, **74**, 6565–6589.

Day, J. M. D., Walker, R. J., Qin, L. & Rumble, D., III (2012). Late accretion as a natural consequence of planetary growth. *Nature Geoscience*, **5**, 614–617.

Day, J. M. D., Waters, C. L., Schaefer, B. F., Walker, R. J. & Turner, S. (2016). Use of hydrofluoric acid desilicification in the determination of highly siderophile element abundances and re-Pt-Os isotope systematics in mafic-ultramafic rocks. *Geostandards and Geoanalytical Research*, **40**, 49–65.

Day, J. M. D., O'Driscoll, B., Strachan, R. A., Daly, J. S. & Walker, R. J. (2017a). Identification of mantle peridotite as a possible Iapetan ophiolite sliver in south Shetland, Scottish Caledonides. *Journal of the Geological Society*, **174**, 88–92. https://doi.org/10.1144/jgs2016-074.

Day, J. M. D., Walker, R. J. & Warren, J. M. (2017b). ^{186}Os-^{187}Os and highly siderophile element abundance systematics of the mantle revealed by abyssal peridotites and Os-rich alloys. *Geochimica et Cosmochimica Acta*, **200**, 232–254.

D'Errico, M. E., Warren, J. M. & Godard, M. (2016). Evidence for chemically heterogeneous Arctic mantle beneath the Gakkel Ridge. *Geochimica et Cosmochimica Acta*, **174**, 291–312.

Dick, H. J., Lin, J. & Schouten, H. (2003). An ultraslow-spreading class of ocean ridge. *Nature*, **426**, 405–412.

Downey, N. J., Stock, J. M., Clayton, R. W. & Cande, S. C. (2007). History of the Cretaceous Osbourn spreading center. *Journal of Geophysical Research: Solid Earth*(B4), **112**.

Falloon, T. J., Danyushevsky, L. V., Crawford, A. J., Meffre, S., Woodhead, J. D. & Bloomer, S. H. (2008). Boninites and adakites from the northern termination of the Tonga trench: implications for adakite petrogenesis. *Journal of Petrology*, **49**, 697–715.

Fisher, R. L. & Engel, C. G. (1969). Ultramafic and basaltic rocks dredged from the nearshore flank of the Tonga trench. *Geological Society of America Bulletin*, **80**, 1373–1378.

Fitton, J. G. & Godard, M. (2004). Origin and evolution of magmas on the Ontong Java plateau. *Geological Society, London, Special Publications*, **229**, 151–178.

Frisby, C., Bizimis, M. & Mallick, S. (2016). Hf–Nd isotope decoupling in bulk abyssal peridotites due to serpentinization. *Chemical Geology*, **440**, 60–72. https://doi.org/10.1016/j.chemgeo.2016.07.006.

Frost, B.R. & Beard, J.S. (2007). On silica activity and serpentinization. *Journal of petrology*, **48**, 1351–1368.

Fruh-green, G. L., Connolly, J. A. D., Plas, A., Kelley, D. S. & Grobety, B. (2004). Serpentinization of oceanic peridotites: implications for geochemical cycles and biological activity the subseafloor biosphere at mid-ocean ridges. *The Subseafloor Biosphere at Mid-Ocean Ridges*, **144**, 119–136.

Golowin, R., Portnyagin, M., Hoernle, K., Hauff, F., Werner, R. & Garbe-Schönberg, D. (2018). Geochemistry of deep Manihiki plateau crust: implications for compositional diversity of large igneous provinces in the Western Pacific and their genetic link. *Chemical Geology*, **493**, 553–566.

Grevemeyer, I., Ranero, C. R., Flueh, E. R., Kläschen, D. & Bialas, J. (2007). Passive and active seismological study of bending-related faulting and mantle serpentinization at the Middle America trench. *Earth and Planetary Science Letters*, **258**, 528–542. https://doi.org/10.1016/j.epsl.2007.04.013.

Griffin, W. L., O'Reilly, S. Y., Ryan, C. G., Gaul, O. & Ionov, D. A. (1998). Secular variation in the composition of subcontinental lithospheric mantle: geophysical and geodynamic implications. *Structure and Evolution of the Australian Continent*, **26**, 1–26.

Guillot, S. & Hattori, K. (2013). Serpentinites: essential roles in geodynamics, arc volcanism, sustainable development, and the origin of life. *Elements*, **9**, 95–98.

Hanghøj, K., Kelemen, P. B., Hassler, D. & Godard, M. (2010). Composition and genesis of depleted mantle peridotites from the Wadi Tayin Massif, Oman ophiolite; major and trace element geochemistry, and Os isotope and PGE systematics. *Journal of Petrology*, **51**, 201–227.

Harvey, J., Gannoun, A., Burton, K. W., Rogers, N. W., Alard, O. & Parkinson, I. J. (2006). Ancient melt extraction from the oceanic upper mantle revealed by re-Os isotopes in abyssal peridotites from the Mid-Atlantic ridge. *Earth and Planetary Science Letters*, **244**, 606–621.

Harvey, J., Garrido, C. J., Savov, I., Agostini, S., Padrón-Navarta, J. A., Marchesi, C., Sánchez-Vizcaíno, V. L. & Gómez-Pugnaire, M. T. (2014). ^{11}B-rich fluids in subduction zones: the role of antigorite dehydration in subducting slabs and boron isotope heterogeneity in the mantle. *Chemical Geology*, **376**, 20–30.

Harvey, J., König, S. & Luguet, A. (2015). The effects of melt depletion and metasomatism on highly siderophile and strongly chalcophile elements: S–se–Te–re–PGE systematics of peridotite xenoliths from Kilbourne hole, New Mexico. *Geochimica et Cosmochimica Acta*, **166**, 210–233.

Hellebrand, E., Snow, J. E., Dick, H. J. B. & Hofmann, A. W. (2001). Coupled major and trace elements as indicators of the extent of melting in mid-ocean-ridge peridotites. *Nature*, **410**, 677–681.

Hirschmann, M. M., Ghiorso, M. S., Wasylenki, L. E., Asimow, P. D. & Stolper, E. M. (1998). Calculation of peridotite partial melting from thermodynamic models of minerals and melts. *I. Review of methods and comparison with experiments*. *Journal of Petrology*, **39**, 1091–1115.

Jackson, M.G., Shirey, S.B., Hauri, E.H. Kurz, M.D. & Rizo, H. (2016). Peridotite xenoliths from the Polynesian Austral and Samoa hotspots: Implications for the destruction of ancient 187Os and 142Nd isotopic domains and the preservation of Hadean 129Xe in the modern convecting mantle. *Geochimica et Cosmochimica Acta*, **185**, 21–43.

Hyndman, R. D. & Peacock, S. M. (2003). Serpentinization of the forearc mantle. *Earth and Planetary Science Letters*, **212**, 417–432.

Kelley, K. A. & Cottrell, E. (2009). Water and the oxidation state of subduction zone magmas. *Science*, **325**, 605–607.

Kelley, K. A., Plank, T., Farr, L., Ludden, J. & Staudigel, H. (2005). Subduction cycling of U, Th, and Pb. *Earth and Planetary Science Letters*, **234**, 369–383.

Kepezhinskas, P. & Defant, M. J. (2001). Nonchondritic Pt/Pd ratios in arc mantle xenoliths: evidence for platinum enrichment in depleted island-arc mantle sources. *Geology*, **29**, 851–854.

Kodolányi, J. Pettke, T., Spandler, C. Kamber, B.S. & Gméling, K. (2012). Geochemistry of ocean floor and fore-arc serpentinites: constraints on the ultramafic input to subduction zones. *Journal of Petrology*, **53**, 235–270.

Lassiter, J.C. & Hauri, E.H. (1998). Osmium-isotope variations in Hawaiian lavas: evidence for recycled oceanic lithosphere in the Hawaiian plume. *Earth and Planetary Science Letters*, **164**, 483–496.

Lassiter, J. C., Byerly, B. L., Snow, J. E. & Hellebrand, E. (2014). Constraints from Os-isotope variations on the origin of Lena trough abyssal peridotites and implications for the composition and evolution of the depleted upper mantle. *Earth and Planetary Science Letters*, **403**, 178–187. https://doi.org/10.1016/j.epsl.2014.05.033.

Lee, C.-T. A., Leeman, W. P., Canil, D. & Li, Z.-X. A. (2005). Similar V/Sc systematics in MORB and arc basalts: implications for the oxygen fugacities of their mantle source regions. *Journal of Petrology*, **46**, 2313–2336.

Li, J., Kornprobst, J., Vielzeuf, D. & Fabriès, J. (1995). An improved experimental calibration of the olivine–spinel geothermometer. *Chinese Journal of Geochemistry*, **14**, 68–77.

Liu, C. Z., Snow, J. E., Brügmann, G., Hellebrand, E. & Hofmann, A. W. (2009). Non-chondritic HSE budget in Earth's upper mantle evidenced by abyssal peridotites from Gakkel ridge (Arctic Ocean). *Earth and Planetary Science Letters*, **283**, 122–132. https://doi.org/10.1016/j.epsl.2009.04.002.

Liu, C.-Z., Xu, Y. & Wu, F.-Y. (2018). Limited recycling of crustal osmium in forearc mantle during slab dehydration. *Geology*, **46**, 239–242.

Lorand, J.-P. & Luguet, A. (2016). Chalcophile and siderophile elements in mantle rocks: trace elements controlled by trace minerals. *Reviews in Mineralogy and Geochemistry*, **81**, 441–488.

Luguet, A. & Reisberg, L. (2016). Highly siderophile element and ^{187}Os signatures in non-cratonic basalt-hosted peridotite xenoliths: unravelling the origin and evolution of the post-Archean lithospheric mantle. *Reviews in Mineralogy and Geochemistry*, **81**, 305–367.

Malvoisin, B. (2015). Mass transfer in the oceanic lithosphere: serpentinization is not isochemical. *Earth and Planetary Science Letters*, **430**, 75–85.

McDonough, W. F. & Sun, S. S. (1995). The composition of the earth. *Chemical Geology*, **120**, 223–253.

Meffre, S., Falloon, T.J., Crawford, T.J., Hoernle, K. Hauff, F., Duncan, R.A., Bloomer, S.H., Wright, D.J. (2012). Basalts erupted along the Tongan fore arc during subduction initiation: evidence from geochronology of dredged rocks from the Tonga fore arc and trench. *Geochemistry, Geophysics, Geosystems, Q12003*, https://doi.org/10.10129/2012GC004335.

Meisel, T. & Horan, M. F. (2016). Analytical methods for the highly siderophile elements. *Reviews in Mineralogy and Geochemistry*, **81**, 89–106.

Meisel, T., Walker, R. J., Irving, A. J. & Lorand, J. P. (2001). Osmium isotopic compositions of mantle xenoliths: a global perspective. *Geochimica et Cosmochimica Acta*, **65**, 1311–1323.

Mercier, J. C. & Nicolas, A. (1975). Textures and fabrics of upper-mantle peridotites as illustrated by xenoliths from basalts. *Journal of Petrology*, **16**, 454–487.

Mével, C. (2003). Serpentinization of abyssal peridotites at mid-ocean ridges. *Comptes Rendus Geosciences*, **335**, 825–852. https://doi.org/10.1016/j.crte.2003.08.006.

Mukhopadhyay, S. & Parai, R. (2019). Noble gases: a record of Earth's evolution and mantle dynamics. *Annual Review of Earth and Planetary Sciences*, **47**, 389–419.

McCarthy, A., Chelle-Michou, C., Müntener, O., Arculus, R. & Blundy, J. (2018). Subduction initiation without magmatism: the case of the missing Alpine magmatic arc. *Geology*, **46**, 1059–1062.

Müntener, O. & Manatschal, G. (2006). High degrees of melt extraction recorded by spinel harzburgite of the Newfoundland margin: the role of inheritance and consequences for the evolution of the southern North Atlantic. *Earth and Planetary Science Letters*, **252**, 437–452.

Niu, Y. (2004). Bulk-rock major and trace element compositions of abyssal peridotites: implications for mantle melting, melt extraction and post-melting processes beneath mid-ocean ridges. *Journal of Petrology*, **45**, 2423–2458. https://doi.org/10.1093/petrology/egh068.

O'Driscoll, B. & González-Jiménez, J. M. (2016). Petrogenesis of the platinum-group minerals. *Reviews in Mineralogy and Geochemistry*, **81**, 489–578.

O'Driscoll, B., Day, J. M. D., Walker, R. J., Daly, J. S., McDonough, W. F. & Piccoli, P. M. (2012). Chemical heterogeneity in the upper mantle recorded by peridotites and chromitites from the Shetland ophiolite complex, Scotland. *Earth and Planetary Science Letters*, **333**, 226–237.

O'Driscoll, B., Walker, R. J., Day, J. M. D., Ash, R. D. & Daly, J. S. (2015). Generations of melt extraction, melt–rock interaction and high-temperature Metasomatism preserved in peridotites of the∼ 497 ma Leka ophiolite complex. *Journal of Petrology*, **56**, 1797–1828.

Paquet, M., Day, J. M. D., Brown, D. B. & Waters, C. L. (2021). Effective global mixing of the highly siderophile elements into Earth's mantle inferred from oceanic abyssal peridotites. *Geochimica et Cosmochimica Acta*. **316**, 347–362. https://doi.org/10.1016/j.gca.2021.09.033.

Parkinson, I. J. & Pearce, J. A. (1998). Peridotites from the Izu-Bonin-Mariana Forearc (ODP leg 125): evidence for mantle melting and melt-mantle interaction in a supra-subduction zone setting. *Journal of Petrology*, **39**, 1577–1618.

Parkinson, I. J., Hawkesworth, C. J. & Cohen, A. S. (1998). Ancient mantle in a modern arc: Osmium isotopes in Izu-Bonin-Mariana forearc peridotites. *Science*, **281**, 2011–2013.

Parkinson, I. J., Arculus, R. J. & Eggins, S. M. (2003). Peridotite xenoliths from Grenada, Lesser Antilles Island arc. *Contributions to Mineralogy and Petrology*, **146**, 241–262.

Paulick, H., Bach, W., Godard, M., De Hoog, J. C. M., Suhr, G. & Harvey, J. (2006). Geochemistry of abyssal peridotites (Mid-Atlantic Ridge, 15°20'N, ODP leg 209): implications for fluid/rock interaction in slow spreading environments. *Chemical Geology*, **234**, 179–210. https://doi.org/10.1016/j.chemgeo.2006.04.011.

Pearce, J.A. Barker, P.F., Edwards, S.J. Parkinson, I.J. & Leat, P.T. (2000). Geochemistry and tectonic significance of peridotites from the South Sandwich arc-basin system, South Atlantic. *Contributions to Mineralogy and Petrology*, **139**, 36–53.

Pettke, T., Kodolányi, J. & Kamber, B. S. (2018). From ocean to mantle: new evidence for U-cycling with implications for the HIMU source and the secular Pb isotope evolution of Earth's mantle. *Lithos*, **316**, 66–76.

Pouchou, J. L. & Pichoir, F. (1987). Basic expression of "PAP" computation for quantitative EPMA. *Proceedings of ICXOM*, **11**, 249–253.

Rampone, E., Hofmann, A. W. & Raczek, I. (1998). Isotopic contrasts within the internal Liguride ophiolite (N. Italy): the lack of a genetic mantle–crust link. *Earth and Planetary Science Letters*, **163**, 175–189.

Righter, K., Chesley, J. T. & Ruiz, J. (2002). Genesis of primitive, arc-type basalt: constraints from Re, Os, and Cl on the depth of melting and role of fluids. *Geology*, **30**, 619–622.

Saha, A., Basu, A. R., Jacobsen, S. B., Poreda, R. J., Yin, Q. Z. & Yogodzinski, G. M. (2005). Slab devolatilization and Os and Pb mobility in the mantle wedge of the Kamchatka arc. *Earth and Planetary Science Letters*, **236**, 182–194.

Sanfilippo, A., Salters, V., Tribuzio, R. & Zanetti, A. (2019). Role of ancient, ultra-depleted mantle in Mid-Ocean-Ridge magmatism. *Earth and Planetary Science Letters*, **511**, 89–98.

Schulze, D. J. (1986). Calcium anomalies in the mantle and a subducted metaserpentinite origin for diamonds. *Nature*, **319**, 483–485.

Schulte, R. F., Schilling, M., Horan, M. F., Anma, R., Komiya, T., Farquhar, J., Piccoli, P. M., Pitcher, L. & Walker, R. J. (2009). Chemical and chronologic complexity in the convecting upper mantle: evidence from the Taitao Ophiolite, southern Chile. *Geochimica et Cosmochimica Acta*, **73**, 5793–5819.

Secchiari, A., Gleissner, P., Li, C., Goncharov, A., Milke, R., Becker, H., Bosch, D. & Montanini, A. (2020). Highly siderophile and chalcophile element behaviour in abyssal-type and supra-subduction zone mantle: New insights from the New Caledonia ophiolite. *Lithos*, **354**, 105338.

Seyler, M., Lorand, J. P., Dick, H. J. & Drouin, M. (2007). Pervasive melt percolation reactions in ultra-depleted refractory harzburgites at the Mid-Atlantic Ridge, 15 20′ N: ODP hole 1274A. *Contributions to Mineralogy and Petrology*, **153**, 303–319.

Shirey, S. B. & Walker, R. J. (1998). The re–Os isotope system in cosmochemistry and high-temperature geochemistry. *Annual Reviews in Earth and Planetary Science*, **26**, 423–500.

Simon, N. S. C., Neumann, E.-R., Bonadiman, C., Coltorti, M., Delpech, G., Grégoire, M. & Widom, E. (2008). Ultra-refractory domains in the oceanic mantle lithosphere sampled as mantle xenoliths at Ocean Islands. *Journal of Petrology*, **49**, 1223–1251.

Snortum, E. & Day, J. M. D. (2020). Forearc origin for coast range ophiolites inferred from osmium isotopes and highly siderophile elements. *Chemical Geology*, **550**, 119723.

Snortum, E., Day, J. M. D. & Jackson, M. G. (2019). Pacific lithosphere evolution inferred from Aitutaki mantle xenoliths. *Journal of Petrology*, **60**, 1753–1772.

Snow, J. E. & Dick, H. J. (1995). Pervasive magnesium loss by marine weathering of peridotite. *Geochimica et Cosmochimica Acta*, **59**, 4219–4235.

Snow, J. E. & Reisberg, L. (1995). Os isotopic systematics of the MORB mantle: Results from altered abyssal peridotites. *Earth and Planetary Science Letters*, **133**, 411–421.

Stagno, V. & Fei, Y. (2020). The redox boundaries of Earth's interior. *Elements*, **16**, 167–172.

Taylor, B. (2006). The single largest oceanic plateau: Ontong Java–Manihiki–Hikurangi. *Earth and Planetary Science Letters*, **241**, 372–380.

Todd, E., Gill, J. B. & Pearce, J. A. (2012). A variably enriched mantle wedge and contrasting melt types during arc stages following subduction initiation in Fiji and Tonga, Southwest Pacific. *Earth and Planetary Science Letters*, **335–336**, 180–194.

Traver, C. (2013) *A petrological and geochemical study of mantle and crystal xenoliths from Lanzarote*. Canary Islands: Unpublished M.S. Thesis, University of California, San Diego, p. 83.

Wang, J., Hattori, K. H., Li, J. & Stern, C. R. (2008). Oxidation state of Paleozoic subcontinental lithospheric mantle below the Pali Aike volcanic field in southernmost Patagonia. *Lithos*, **105**, 98–110.

Wang, J., Hattori, K. & Xie, Z. (2013). Oxidation state of lithospheric mantle along the northeastern margin of the North China craton: implications for geodynamic processes. *International Geology Review*, **55**, 1418–1444.

Warren, J. M. (2016). Global variations in abyssal peridotite compositions. *Lithos*, **248**, 193–219.

Widom, E., Kepezhinskas, P. & Defant, M. (2003). The nature of metasomatism in the sub-arc mantle wedge: evidence from Re-Os isotopes in Kamchatka peridotite xenoliths. *Chemical Geology*, **196**, 283–306.

Woodland, A. B., Gräf, C., Sandner, T., Höfer, H. E., Seitz, H. M., Pearson, D. G. & Kjarsgaard, B. A. (2021). Oxidation state and metasomatism of the lithospheric mantle beneath the Rae Craton, Canada: strong gradients reflect craton formation and evolution. *Scientific Reports*, **11**, 1–10.

Workman, R. K. & Hart, S. R. (2005). Major and trace element composition of the depleted MORB mantle (DMM). *Earth and Planetary Science Letters*, **231**, 53–72.

Wright, D. J., Bloomer, S. H., MacLeod, C. J., Taylor, B. & Goodlife, A. M. (2000). Bathymetry of the Tonga trench and forearc: a map series. *Marine Geophysical Researches*, **21**, 489–511.

Xiong, Y. & Wood, S. A. (2000). Experimental quantification of hydrothermal solubility of platinum-group elements with special reference to porphyry copper environments. *Mineralogy and Petrology*, **68**, 1–28.

Deltech Furnaces

Sustained operating temperatures to 1800° Celsius

www.deltechfurnaces.com

Gas Mixing System

An ISO 9001:2015 certified company

Custom Vertical Tube

ASME NQA-1 2008 Nuclear Quality Assurance

Standard Vertical Tube

Control systems are certified by Intertek UL508A compliant

Bottom Loading Vertical Tube